

# High-speed bounding with the MIT Cheetah 2: Control design and experiments

The International Journal of  
Robotics Research  
2017, Vol. 36(2) 167–192  
© The Author(s) 2017  
Reprints and permissions:  
[sagepub.co.uk/journalsPermissions.nav](http://sagepub.co.uk/journalsPermissions.nav)  
DOI: 10.1177/0278364917694244  
[journals.sagepub.com/home/ijr](http://journals.sagepub.com/home/ijr)



Hae-Won Park<sup>1</sup>, Patrick M Wensing<sup>2</sup>, and Sangbae Kim<sup>2</sup>

## Abstract

This paper presents the design and implementation of a bounding controller for the MIT Cheetah 2 and its experimental results. The paper introduces the architecture of the controller along with the functional roles of its subcomponents. The application of impulse scaling provides feedforward force profiles that automatically adapt across a wide range of speeds. A discrete gait pattern stabilizer maintains the footfall sequence and timing. Continuous feedback is layered to manage balance during the stance phase. Stable hybrid limit cycles are exhibited in simulation using simplified models, and are further validated in untethered three-dimensional bounding experiments. Experiments are conducted both indoors and outdoors on various man-made and natural terrains. The control framework is shown to provide stable bounding in the hardware, at speeds of up to 6.4 m/s and with a minimum total cost of transport of 0.47. These results are unprecedented accomplishments in terms of efficiency and speed in untethered experimental quadruped machines.

## Keywords

Legged robots, motion control, biologically-inspired robots, dynamics

## 1. Introduction

Quadrupedal animals exhibit an unmatched ability to perform high-speed, agile, and robust locomotion. Their morphology affords the ability to traverse unstructured terrains, and their varied gaits provide versatility across a wide range of scenarios in nature. Whether running down a rocky hill or weaving through a dense forest, they are able to move dynamically in even the most challenging environments. Replicating such remarkable mobility and robustness has long been a goal for legged robotics research.

Recent advances in quadrupedal robots have shown a great potential to realize these capabilities. BigDog (Raibert et al., 2008), the legged squad support system (LS3), WildCat, and Spot developed by Boston Dynamics have demonstrated dynamic walking and fast running in outdoor environments with great robustness. Bounding, trotting, and pronking gaits shown by StarlETH (Gehring et al., 2013, 2014) and trotting gaits in HyQ (Semini et al., 2011, 2015) are other exemplary recent advances in quadrupedal robotic locomotion. Recently, the Massachusetts Institute of Technology (MIT) Cheetah robots have achieved efficient trotting in planar experiments (Hyun et al., 2014; Seok et al., 2015) and dynamic bounding in untethered 3D tests (Park et al., 2014, 2015a), with results of this current work shown in Figure 1.

Various approaches in model-based control system design substantially contributed to such advancement. The work at University of Southern California (USC) on Little Dog demonstrated the importance of managing force interactions within the technical framework of floating-base inverse dynamics (Righetti et al., 2013). The distribution of foot forces has also been shown to benefit operational-space control of more dynamic gaits, including recent results for quadruped trotting (Palmer and Orin, 2007; Wensing et al., 2015). In the control systems of StarlETH, hierarchical operational-space control has been employed specifically considering the effects of contact interactions on the presence of underactuation in the constrained system dynamics (Hutter et al., 2014b). Footstep planning in this platform (Hutter, 2013) has been inspired by a spring-loaded inverted pendulum (SLIP) based (Blickhan and Full, 1993) methods, similar to those introduced by Raibert (1986). These planned motions have then been encoded in the robot

<sup>1</sup>Department of Mechanical Engineering and Science, University of Illinois at Urbana Champaign, USA

<sup>2</sup>Department of Mechanical Engineering, Massachusetts Institute of Technology, USA

## Corresponding author:

Hae-Won Park, University of Illinois at Urbana Champaign, 105 South Mathews Avenue, 2144 MEL, Urbana, IL 61801, USA.  
Email: haewon@illinois.edu

through solutions of a constrained operational-space control problem – a problem also commonly addressed in the humanoid robot community (Park and Khatib, 2006; Sentis et al., 2010). With this approach, researchers at ETH Zurich have successfully achieved dynamic trotting with speeds of up to 0.7 m/s (Froude number<sup>1</sup> of 0.12) in StarlETH. The robot has achieved a minimum total cost of transport of 1.7 in a trotting gait at 0.5 m/s (Hutter et al., 2014a).

Other dynamic trotting gaits have been demonstrated by Barasuol et al. (2013) for the hydraulic robot HyQ using bio-inspired nonlinear oscillators. Desired trajectories of the robot's foot were calculated by employing a central pattern generator (CPG) and implemented using feedforward torques from floating-base inverse dynamics with Proportional-Derivative (PD) control. Currently, HyQ is able to run with a speed of 2.0 m/s (Froude number of 0.42) with off-board power. As opposed to StarlETH, which includes physical springs in its actuators, the control of HyQ uses active impedance control (Hogan, 1985) of its passively stiff hydraulics to compliantly handle impacts and environmental disturbances.

The development of gait-specific controllers across these robots has begun to enable great versatility in the locomotion capabilities of modern quadrupeds. Walking control in Little Dog has served as a foundation for learning algorithms, applied to foothold selection, to traverse a variety of uneven terrains (Kalakrishnan et al., 2011). In HyQ, walking algorithms have been integrated with the Microsoft Kinect (Winkler et al., 2014) and stereo vision (Bazeille et al., 2014) to enable the negotiation of irregular terrain. Reliable gait-level control architectures will continue to be important building blocks for this emerging class of robots.

In this paper, control for the MIT Cheetah is based in large part on realizing feedforward force profiles at the contact interface. This strategy for the Cheetah is enabled in-part by its proprioceptive force control actuators, which deliver high-fidelity control of ground applied forces. The Cheetah robot includes high air-gap radius brushless Direct Current (DC) motors which enable the use of low-gear-ratio reductions, prevents the need for series compliance, and improves motor torque density and force bandwidth (Seok et al., 2012; Wensing et al., 2016). This unique actuation scheme provides high-fidelity rendering of desired forces at the foot without requiring foot force sensors and has a force bandwidth of 100 Hz. This high-bandwidth authority allows the control design presented here to view the ground reaction forces effectively as control inputs. This feature helps to simplify the design and regulation of limit cycles for running across a range of speeds from 0 – 6.4 m/s, with a maximum Froude number of 7.1.

This performance across speed is significant, as most published control algorithms have still only demonstrated gaits in a slow speed range (Froude numbers below 1.3). In order to obtain running with different speeds, control parameters have had to be re-obtained by hand tuning or iterative and computationally expensive optimization processes (Coros et al., 2011; Herr and McMahon, 2001; Hyun

et al., 2014). This need for detailed tuning makes it further difficult for robots to transition stably between adjacent controllers for two different speeds.

Work in this paper shows the capability of impulse-scaling principles, in particular to automatically adapt control across speeds without the need for parameter retuning. The main idea behind impulse scaling is that the vertical impulse from gravity is counteracted through an equal and opposite vertical contact impulse during a period of stance. Indeed, an unavoidable consequence of fundamental physics dictates that, in the long run, the average net vertical contact force must balance gravity for the momentum to remain bounded. Further, periodic gaits must admit impulse balance from step to step. The use of impulse scaling to generate physics-based feedforward force profiles across speeds has been an important departure from our previous work, which used high-impedance position control to perform 2D-constrained trotting with the MIT Cheetah 1 (Hyun et al., 2014). Through impulse scaling, the gait in this current work is dominantly created with feedforward forces, enabling robust locomotion in 3D over a range of terrains and speeds.

### *1.1. Contribution*

The main contribution of the paper is to present a control design process that has enabled untethered 3D bounding in the MIT Cheetah 2 at speeds from 0–6.4 m/s without retuning any control parameters. The algorithms developed through this process, in a sense, bridge the gap between heavily model-based methods (Hutter et al., 2014b) and model-free heuristic methods (Raibert, 1986). In order to promote applicability to dynamic experiments, where exact dynamic model details are difficult to obtain, we instead focus on a reduced set of model-based control actions which address the most salient aspects of locomotion. Namely, this includes selecting ground reaction force patterns, which admit zero net linear and angular impulse from step to step. While exact model-based details may be difficult to identify, parameters which roughly determine the effects of these momentum profiles are easily identifiable as aggregate parameters (total mass, lumped rotational inertia) of the machine. It is conjectured that this macro view of the control problem has promoted the success of the experimental implementation of our algorithm.

Portions of the contents in this article have appeared previously in other publications by the authors. A preliminary version of the vertical impulse scaling principles (Section 4) appeared in the work by Park and Kim (2015). These ideas have led to experimentally verified controllers as applied in place bounding (Park et al., 2014) and variable-speed running (Park et al., 2015b), which have appeared at recent conferences. These conference contributions have reformulated the control originally presented by Park and Kim (2015) to include only the most important components of model-based control. This article builds from the work by

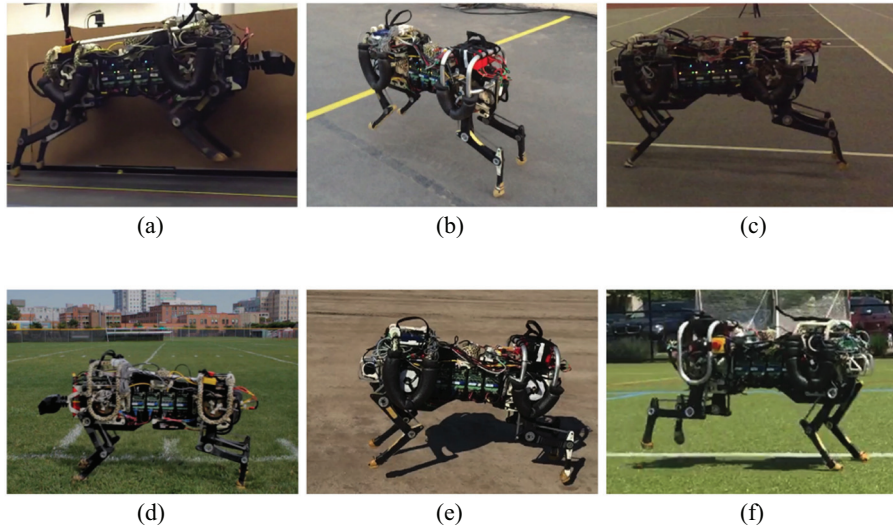


**Fig. 1.** MIT Cheetah 2 running on a variety of terrains without any tethers or support. The control system described in this work enables the robot to stably accelerate from 0.0 m/s up to 6.4 m/s with a minimum total cost of transport of 0.47. A snapshot of the maximum speed gait is given in subfigure (a) Treadmill; (b) Paved surface; (c) Indoor track; (d) Grassy field; (e) Dirt track; (f) Artificial turf field.

Park et al. (2014) and Park and Kim (2015) and provides an updated version of the controller which has enabled the platform to reach a speed of 6.4 m/s (Froude number of  $Fr = 7.1$ ). We further expand upon these previous conference papers, present additional analyses of the control system stability, and describe additional implementation details which have been necessary to transition the simulation work by Park and Kim (2015) into a controller which enables robust high-speed running experiments.

## 1.2. Organization

The remainder of the paper is organized as follows. Section 2 briefly overviews the control design process and Section 3 describes a simple hybrid bounding model that is extensively used throughout the study. Section 4 introduces the impulse scaling principles used to generalize nominal force profiles across a range of speeds. Periodic orbits are guaranteed to exist for our controller parameterization when vertical and angular momentum are conserved from step to step. However, when force profiles for bounding are executed in purely open loop, such limit cycles are guaranteed to be unstable. The instability is remedied through the addition of two main components, impedance-based feedback and a gait pattern stabilizer as described in Section 5. Section 6 describes a series of control system details which are important to the implementation of the algorithm in hardware. Results of the bounding experiments are described in Section 7 and further discussed in Section 8. Section 9 provides concluding remarks. Notation is described in Appendix 2, with three other main appendices providing formal proof of the existence of periodic orbits in the simple hybrid bounding model, the instability of these orbits in open-loop, and asymptotic stability of the gait timing under an intuitive gait pattern stabilizer design.

## 2. Overview of the control design process

This section provides an overview of the control design process for the bounding gait of the MIT Cheetah 2. The control design process is divided into a sequence of three steps, shown in Figure 2:

- (a) impulse-based gait design that provides periodic orbits across a wide range of speeds;
- (b) gait stabilization to add feedback on top of the periodic orbits;
- (c) incorporation of implementation details that take into account complex details of the hardware platform which are not captured in the simple bounding models.

Each control design step is pursued for a corresponding system model as described in Figure 2. The system models that are considered in the process are:

- (a) a time-switched model;
- (b) an event-switched model;
- (c) the hardware platform itself.

When proceeding to each next control design process step, more control components are added on top of the previous design to address increasingly complex dynamic characteristics. This sequential design process allows control based on fundamental principles to be developed on the simplest models, while realized in the full complexity of the hardware. In a sense, this design methodology is philosophically in line with the templates and anchors hypothesis of neuromechanical locomotor control (Full and Koditschek, 1999).

The most fundamental step in the control design process, impulse-based gait design, is proposed based on the simplest time-switched model. In the time-switched model,

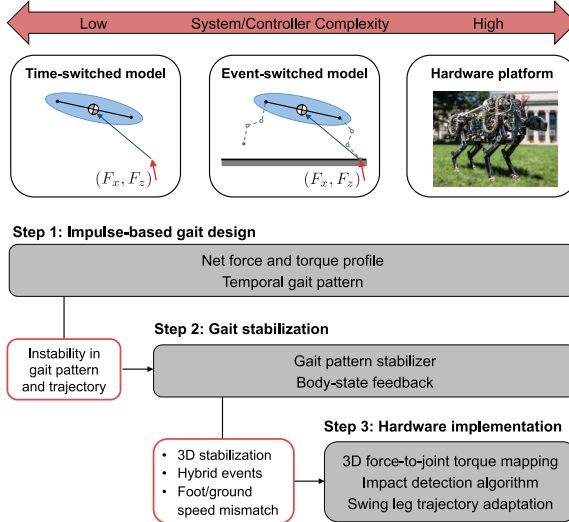


**Fig. 2.** Proposed sequential control design process to take into account the complexity of the experimental platform. The process has three main steps. It starts with impulse-based gait design as introduced in Section 4, is followed by gait stabilization as described in Section 5, and ends with incorporation of implementation details as given in Section 6. Each design step is carried out with a corresponding system model that provides a hierarchical level of abstraction. The challenges addressed by each following step are outlined in red.

the robot is represented as a single rigid body with ground reaction forces acting on the body as an external force at a virtual foot point. This model captures the fact that contact forces (ground reaction forces) are the only external forces which are able to shape the motions of the center of mass of the mobile articulated system (Ostrowski and Burdick, 1996; Wieber, 2006). For each running speed, a temporal gait pattern is defined, alternating between phases of flight and stance, to assign the scheduling of the ground reaction forces applied to the body. Due to the simplicity of the model and fixed temporal gait pattern for each speed, periodic orbits are guaranteed to exist when impulse scaling principles are followed based on Proposition 1 in Section 4. Application of the impulse scaling provides periodic orbits across a wide range of running speeds in this simplest model. The orbits, however, are proven to be unstable in Corollary 1 when driven by open-loop force profiles alone.

The next step in the control design is gait stabilization, as explained in Section 5, which adds discrete and continuous feedback on top of the periodic orbits obtained in the previous step. For this step, an event-switched hybrid model is introduced wherein the effects of swing leg motion on gait timing are added for closer approximation of the hardware platform. In this model, transitions from flight to stance occur when the vertical position of the swing foot crosses the ground plane. Two main components, continuous body-state feedback and a discrete gait pattern stabilizer, are

introduced. The body-state feedback is included to promote convergence to a nominal trajectory during stance, while the gait pattern stabilizer is introduced to enforce the temporal gait pattern. The stability of the system is analyzed and verified with the event-switched hybrid model.

The final step is the addition of platform-specific details to take into account the complex nature of the experimental robot, which are not addressed in the above conceptual models. Section 6 introduces a method to compute joint torques which provide the designed forces from the conceptual models. Since the simple models do not include leg mass, this section also describes methods for online modification of the swing leg trajectories to address practical considerations of ground and foot speed matching around hybrid transitions.

The first two steps of the control design, the impulse-based gait design and gait stabilization, use simple hybrid models extensively in design and validation. The following section provides a detailed specification of the time-switched hybrid model which is used to develop an impulse-based gait.

### 3. A time-switched hybrid system model of bounding

#### 3.1. Hybrid system model

In a quadrupedal bounding gait, the front and hind leg pairs act in parallel. As a result, the quadruped can be modeled as a two-legged system in the sagittal plane, as shown in Figure 3. The model alternates between phases of stance and flight, and between periods of front and back stance.

The dynamics of this simple model can be described as a hybrid system, with periods of continuous dynamics punctuated by discrete maps. The front stance phase (numbered 1) is modeled with only the front leg in contact with the ground, the first aerial phase (numbered 2) has both legs in the air, the back stance phase (numbered 3) has only the back leg in contact with the ground, and the second aerial phase (numbered 4) has both legs airborne. Other cases, such as double support phases where both the front and back pairs of legs are in contact, as well as other transitions, are not considered in the analysis with this simplified bounding gait model. Section 6 provides a practical solution to handle these other transitions which may occur in the hardware. Each numbered phase  $j$  ends when the system reaches a guard set  $S_j$  and subsequently follows a discrete map  $\Delta_j$  to transition to the next state. Further details of the model are provided in the paragraphs to follow.

#### 3.2. Coordinates and actuation

Across each phase, the configuration space for the model is abstracted as  $Q = SE(2)$ . This abstraction is made considering an assumption of massless legs. Within each phase, the configuration is described in coordinates

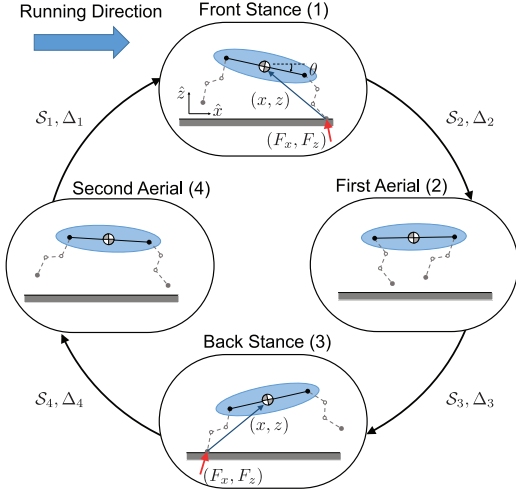


**Fig. 3.** A simplified hybrid quadrupedal bounding model. Assuming massless legs, the quadruped is abstracted by a planar rigid body evolving under the influence of ground reaction forces and gravity. A fixed horizontal foot placement relative to the hip at the beginning of a stance is used to determine the point of application for the ground reaction force.

as  $\mathbf{q} = (x, z, \theta) \in \mathcal{Q}$ , where  $x$  ( $z$ )  $\in \mathbb{R}$  locates the horizontal (vertical) position of the center of mass (CoM) relative to the most recent/current stance foot, and  $\theta$  provides the pitch angle of the body (clockwise positive) relative to the horizontal about a  $\hat{y}$  axis into the page. Further details are provided in Figure 3.

Under the assumption of massless legs, the forces/momenta exerted by each leg onto the body are statically equivalent to the horizontal and vertical ground reaction forces  $F_x$  and  $F_z$  on the foot in stance.<sup>2</sup> As a result, sets of admissible controls for each phase are described by

$$\mathcal{U}_2 = \mathcal{U}_4 := \{(0, 0)\} \quad (1)$$

$$\mathcal{U}_1 = \mathcal{U}_3 := \{(F_x, F_z) \text{ s.t. } |F_x| \leq \mu F_z\} \quad (2)$$

where  $\mu \in \mathbb{R}_+$  is the coefficient of friction. Although these forces are not direct control inputs for the robot, in practice, the design of the Cheetah enables effective proprioceptive control of the ground reaction forces without the need for force sensing at the foot (Wensing et al., 2016).

### 3.3. Domains, guards, and reset maps

In this simple model, transitions between states are assumed to happen on a pre-defined timing schedule. That is, after entering each state  $j$ , the system transitions to the adjacent state after a pre-defined dwell time  $T_j \in \mathbb{R}_+$ . To capture this characterization, the continuous dynamics in each phase take place on  $\mathcal{D}_j := T\mathcal{Q} \times \mathbb{R}_+$  with  $\mathbf{x} := (\mathbf{q}, \dot{\mathbf{q}}, \bar{t})$ , where  $\bar{t}$  represents the current dwell time. Under this specification, the guard sets are given as  $\mathcal{S}_j = \{(\mathbf{q}, \dot{\mathbf{q}}, \bar{t}) \text{ s.t. } \bar{t} = T_j\}$ . The total time to complete one full cycle is specified as  $T = \sum_j T_j$ .

Reset maps following each stance state follow an identical structure

$$\Delta_j(\mathbf{x}) := (\mathbf{q}, \dot{\mathbf{q}}, 0)$$

for  $j \in \{1, 3\}$ . Following each flight state, the reset maps enforce a fixed initial horizontal offset  $x_0^f$  of the stance foot relative to the current stance hip. Thus, for  $j \in \{2, 4\}$

$$\Delta_j(\mathbf{x}) := (\mathbf{q}^+, \dot{\mathbf{q}}, 0)$$

where  $\mathbf{q}^+ = (x^+, z, \theta)$ , and the new horizontal position  $x^+$  follows

$$x^+ = \begin{cases} \frac{\ell}{2} \cos(\theta) - x_0^f & \text{if } j = 2 \\ -\frac{\ell}{2} \cos(\theta) + x_0^f & \text{if } j = 4 \end{cases}$$

The quantity  $\ell \in \mathbb{R}_+$  represents the distance between the two hips of the quadruped. Note that due to the assumption of massless legs,  $\dot{\mathbf{q}}$  remains unchanged. This update law assumes that the CoM of the robot is located in the middle of the body.

### 3.4. Effects of controls

The dynamics of the system can be described using the same equations of motion across each phase. The dynamic equations take a simple form

$$\begin{aligned} m \ddot{\mathbf{p}} &= \mathbf{F} + m \mathbf{a}_g \\ I \ddot{\theta} &= \mathbf{F} \wedge \mathbf{p} \\ \dot{\bar{t}} &= 1 \end{aligned} \quad (3)$$

where,  $\mathbf{p} = (x, z)^T$ ,  $\mathbf{F} = (F_x, F_z)^T$ , and  $\mathbf{a}_g = (0, -g)^T$  is the gravitational acceleration vector.  $\wedge$  is the wedge product<sup>3</sup> defined by  $a \wedge b := a_2 b_1 - a_1 b_2$  and  $\mathbf{F} \wedge \mathbf{p}$  is the moment at the center of mass from the ground reaction forces. As a result the system dynamics can be written commonly as

$$\dot{\mathbf{x}} = \mathbf{f}(\mathbf{x}) + \mathbf{g}(\mathbf{x}) \mathbf{F} \quad (4)$$

### 3.5. Simple model parameters

Throughout the paper, the model parameters  $m$ ,  $I$ , and  $\ell$  used are estimated from the MIT Cheetah 2 robot. The body's mass  $m$  and inertia  $I$  are assumed to be 31 kg and 2.9 kg · m<sup>2</sup> respectively, with body length  $\ell = 0.7$  m.

### 3.6. Hybrid trajectories

Throughout the paper, any trajectory of the hybrid system will be assumed to start in state  $\mathbf{x}_0 = (\mathbf{q}, \dot{\mathbf{q}}, 0)^T$  in the front stance at  $t = 0$ . Closed-loop feedback controllers are parameterized by a set of parameters  $\Xi$  such that for  $\xi \in \Xi$ ,  $\mathbf{F} := \mathbf{F}(\mathbf{x}, \xi)$ . Notationally,  $\mathbf{x}(t; \mathbf{x}_0, \xi)$  represents the state of the system at time  $t$  given  $\mathbf{x}_0$  as an initial condition. Due to reset maps,  $\mathbf{x}(t; \mathbf{x}_0, \xi)$  is only piecewise  $\mathcal{C}^1$  (continuously differentiable) in time. At any reset time  $\tau$  left and right limits are specified according to  $\mathbf{x}(\tau^-; \mathbf{x}_0, \xi)$  and  $\mathbf{x}(\tau^+; \mathbf{x}_0, \xi)$ , respectively. The dependence of  $\mathbf{x}(t)$  on  $\mathbf{x}_0$  or  $\xi$  is often dropped for convenience when it is not required for clarity.

## 4. Impulse-based gait design

This section describes the impulse-based gait design which parameterizes a class of periodic orbits for the simple hybrid model through arguments based on the first principles of momentum conservation. The use of linear and angular momentum has recently received a great deal of attention in the humanoids community for applications to balance control (Hopkins et al., 2015; Macchietto et al., 2009; Orin et al., 2013; Wensing and Orin, 2016), and to accelerate trajectory optimization (Dai et al., 2014). Momentum warping by hand has also been found to be a powerful tool for motion editing to produce physics-based character animations (Sok et al., 2010). The impulse scaling approach used here is most similar to momentum warping in animation. We note that for any periodic limit cycle, the linear and angular momentum must undergo zero net change from the beginning to the end of the cycle. Warping force trajectories in order to ensure this condition across changes in gait timing enables a impulse-based parameterization of hybrid limit cycles for this system.

### 4.1. An impulse principle in periodic bounding

The ground reaction forces  $\mathbf{F}$  during the front and back stance affect both the linear momentum in the sagittal plane as well as the pitch angular momentum about the CoM. Due to the importance of pitch stabilization during high-speed bounding, a change of variables is applied to the control input  $\mathbf{F} = (F_x, F_z)$ . Letting  $\tau = \mathbf{F} \wedge \mathbf{p}$ , we can instead view  $(\tau, F_z)$  as control inputs when  $z \neq 0$  to more directly control the pitch momentum evolution. Under this change of variables

$$\begin{aligned} m\ddot{x} &= F_x = \frac{x F_z + \tau}{z}, \quad z > 0 \\ m\ddot{z} &= F_z - mg \\ I\ddot{\theta} &= \tau \end{aligned} \tag{5}$$

With the formal description of the system, the following proposition introduces conditions on  $F_z$  and  $\tau$  which are sufficient to admit a periodic orbit for the hybrid system with the continuous dynamics given by equation (5).

**Proposition 1.** *(Existence of a periodic orbit). For the simple hybrid bounding model given by equation (5), suppose that the time-dependent force and torque profiles  $F_z(t)$  and  $\tau(t)$  satisfy*

$$\int_0^T (-mg + F_z(t)) dt = 0 \tag{6}$$

$$\int_0^T \tau(t) dt = 0 \tag{7}$$

$$F_z(t) \geq 0, \quad \forall t \in [0, T] \tag{8}$$

for some constant  $T > 0$ . Then, the hybrid model has a periodic orbit with a period of  $T$ .

*Proof.* The proof is given in Appendix 3.  $\square$

**Remark 1.** Forces  $F_z(t)$  satisfying equation (6) means vertical forces cancel gravity on average, and torques  $\tau(t)$  satisfying equation (7) means the average rotational acceleration is zero. These together imply conservation of vertical linear momentum and pitch angular momentum from step to step. Thus, conservation of momentum in these two directions alone from step to step can be seen as sufficient conditions for the existence of a periodic orbit in this model.

**Remark 2.** While the condition given by equation (8) requires unidirectional forces as inputs, the proposition does not guarantee that the resultant orbit will require lateral forces  $|F_x(t)| \leq \mu F_z(t)$ . Frictional feasibility of the orbits is verified in a post-processing step in this work.

**Remark 3.** Periodicity in the  $x$  coordinate does not imply that the system returns back to an original displacement following its orbit. Rather, since  $x$  measures the position of the CoM relative to the foot, the reset maps  $\Delta_2(\mathbf{x})$  and  $\Delta_4(\mathbf{x})$  reset  $x$  to a value  $x^+$  which is a function of  $\theta$  only and regardless of the exact forward progress.

**Corollary 1.** Any periodic orbit obtained from the result of the open-loop controls  $\tau(t)$  and  $F(t)$  satisfying the conditions of Proposition 1 is orbitally unstable.

*Proof.* The proof is given in Appendix 4.  $\square$

Corollary 1 demonstrates the **necessity of feedback** to stabilize these orbits. This result may come as a surprise to some, as work by Mombaur (2009) demonstrated the existence of open-loop stable running behaviors in more complex (10 degree-of-freedom) articulated characters.

In the following sections, we propose a specific selection of force and torque profiles which satisfy the conditions in Proposition 1 for the existence of periodic orbits. These nominal forces will be used as a feedforward command in the robot, with additional feedback forces as addressed in Section 5.

### 4.2. Gait timing simplifications for bounding

The gait pattern in this work is selected to provide front/back symmetry. That is, at each running speed, the stance durations  $T_1$  and  $T_3$  are set to a common value  $T_{st}$ , while flight durations  $T_2$  and  $T_4$  are set to a common value  $T_{air}$ . For a desired velocity  $v_d$ , the stance time is set as

$$T_{st} = L/v_d \tag{9}$$

where  $L \in \mathbb{R}_+$  represents the stride length and nominally takes a value of  $L = 0.4$  m in experiments (approximately 0.57 of the body length). The duration of the swing time for each leg  $T_{sw} := T_{st} + 2T_{air}$  is chosen to be fixed across

speeds at  $T_{\text{sw}} = 0.22$  s which is taken from the swing duration of the Cheetah and Greyhound during galloping (Hudson et al., 2012; Maes et al., 2008). The two phases of duration  $T_{\text{air}}$  are then calculated as

$$T_{\text{air}} = \frac{T_{\text{sw}} - T_{\text{st}}}{2} \quad (10)$$

#### 4.3. Vertical force profiles: Duty cycle modulation via vertical impulse scaling

This subsection presents the selection of vertical force profiles to modulate the duty cycle of bounding while balancing the net vertical impulse from gravity.

**4.3.1. Selection of force profile.** The vertical forces  $F_z^f$  and  $F_z^b$  are chosen as time-dependent profiles shown in Figure 4(a), which are parametrized as

$$F_z^i := F_z^i(\alpha_z^i, s_{\text{st}}), \quad s_{\text{st}} = \frac{\bar{t}}{T_{\text{st}}} \text{ for } i = f, b \quad (11)$$

where  $\alpha_z^i \in \mathbb{R}_+$  represents the magnitude of the force profile, as depicted in Figure 4(a).  $s_{\text{st}} \in \mathbb{R}_+$  is the normalized phase time representing percentage of the stance phase completed.

The force profile of the front leg, given by equation (11), is made up of two concatenated third-order Bézier polynomials, where the Bézier coefficients are given by

$$\beta_z = \begin{cases} \alpha_z [0.0 \ 0.8 \ 1.0 \ 1.0] & \text{for } s_{\text{st}} \leq s_{\text{peak}} \\ \alpha_z [1.0 \ 1.0 \ 0.8 \ 0.0] & \text{for } s_{\text{st}} > s_{\text{peak}} \end{cases} \quad (12)$$

where,  $s_{\text{peak}} \in (0, 1)$  is a parameter to change the position of the peak. Here, we set  $s_{\text{peak}} = 0.5$  to provide a force profile that is symmetric about midstance, but will adjust this value to  $s_{\text{peak}} = 0.3$  during the running experiments explained in Section 7. The coefficients in equation (12) are chosen to ensure continuity between the two Bézier polynomials up to first order derivatives in time, and for easy scaling of the force profile. To further enforce front/back symmetry of the bounding gait, we fix  $\alpha_z^f = \alpha_z^b = \alpha_z$ .

**4.3.2. Modulation of stance duration.** From the previous section, we can see that only two parameters are required to describe the vertical force profile, the duration of stance  $T_{\text{st}}$ , and the magnitude of the force profile  $\alpha_z$ . Here, we will draw the relation between these two parameters using equation (6), which is rewritten as

$$\int_0^T F_z dt = \int_0^T mg dt = mgT \quad (13)$$

Thus, the physical principle of vertical impulse scaling is that the ground applied vertical impulse must scale with the gait period, irrespective of the time spent in stance. Because the area under any Bézier curve can be simply calculated by

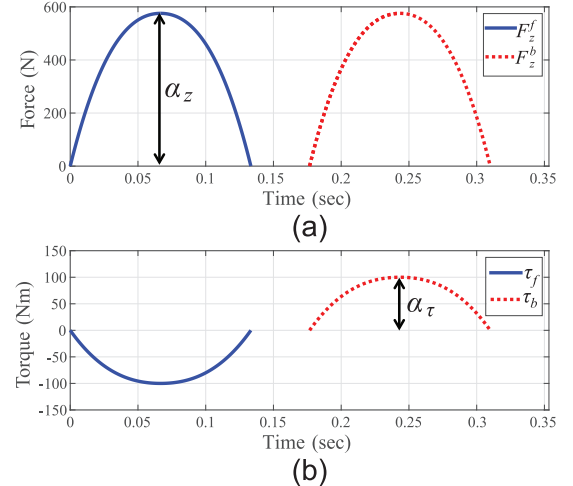


**Fig. 4.** Example force and torque profile shapes that satisfy the conditions in Proposition 1. (a) Force profile (b) Torque profile.

averaging the Bézier coefficients multiplied by the length of duration, equation (13) is rewritten as

$$2c\alpha_z T_{\text{st}} = mgT \quad (14)$$

where the average Bézier coefficient

$$c = \text{mean}[0.0 \ 0.8 \ 1.0 \ 1.0] \quad (15)$$

gives the area under the force profile when  $\alpha_z = 1$  and  $T_{\text{st}} = 1$ . From equation (14),  $\alpha_z$  is then given by

$$\alpha_z = \frac{mgT}{2cT_{\text{st}}} \quad (16)$$

to enforce periodicity in vertical momentum. Equation (16) will be used to calculate the magnitude of the force profile  $\alpha_z$  when  $T_{\text{st}}$  is given. Now, given  $T_{\text{st}}$ , either directly or indirectly through  $v_d$  using equation (9), all remaining parameters associated with the vertical force profile are specified uniquely. Figure 4(a) shows an example of the force profile when  $T_{\text{st}} = 0.133$  s.

**Remark 4.** The principle of vertical impulse scaling should be viewed as designing vertical forces which satisfy equation (13) across changes in gait timing. The choice to fix force profile shape and apply force scaling represents an effective, yet simple, design choice to satisfy equation (13).

#### 4.4. Torque profiles for direct control of pitch oscillation

Pitch torques about the CoM,  $\tau_f$  and  $\tau_b$ , caused by the front and back legs are similarly chosen to be time-dependent profiles as shown in Figure 4(b). These torques are parametrized as

$$\tau_i := \tau_i(\alpha_\tau, s_{\text{st}}), \quad \text{for } i = f, b \quad (17)$$

where,  $\alpha_\tau$  is the magnitude of the torque profile and is applied for both the front and back legs. Torque profiles are selected as concatenated third-order Bézier polynomials, with Bézier coefficients of the front leg given by

$$\beta_\tau^f = \begin{cases} -\alpha_\tau [0.0 \ 0.8 \ 1.0 \ 1.0] & \text{for } s_{st} \leq 0.5 \\ -\alpha_\tau [1.0 \ 1.0 \ 0.8 \ 0.0] & \text{for } s_{st} > 0.5 \end{cases} \quad (18)$$

The Bézier coefficients of the hind leg are given by

$$\beta_\tau^b = \begin{cases} \alpha_\tau [0.0 \ 0.8 \ 1.0 \ 1.0] & \text{for } s_{st} \leq 0.5 \\ \alpha_\tau [1.0 \ 1.0 \ 0.8 \ 0.0] & \text{for } s_{st} > 0.5 \end{cases} \quad (19)$$

Because the areas of the front and back leg torque profiles are equal and opposite, as shown in Figure 4(b), equation (7) is satisfied. In the next section, we will search for periodic orbits for different desired speeds  $v_d$  and torque scalings  $\alpha_\tau$  applied to the simplified model.

**Remark 5.** Note that smaller values for  $\alpha_\tau$  may seem universally desirable, since minimizing  $\alpha_\tau$  minimizes pitch excursion during the gait. However, when  $\alpha_\tau$  is small, ground forces must be angled closer to the center of the body. Thus, reducing  $\alpha_\tau$  increases friction requirements and hip torque requirements. In contrast, high values of  $\alpha_\tau$  increase pitch magnitude and correspondingly increase knee torque requirements through deeper knee bends. Managing these tradeoffs, while satisfying friction limits, is left as a design freedom to the control developer.

#### 4.5. Periodic orbits

The analysis of periodic orbits through the lens of Poincaré has enabled many previous studies on gait analysis and control design within legged locomotion (Poulakakis et al., 2006; Remy et al., 2010; Sreenath et al., 2011). In a similar manner here, the existence and stability of orbits in the hybrid bounding model can be reduced to studying the discrete results of trajectories successively passing through a Poincaré section  $\mathcal{P}$ . The Poincaré section is selected as one of the guards from the hybrid system model

$$\mathcal{P} = \{(\mathbf{q}, \dot{\mathbf{q}}, \bar{t}) \in \mathcal{D}_1 \text{ s.t. } \bar{t} = 0\} \quad (20)$$

We let  $\xi = (v_d, \alpha_\tau)$  represent a vector of parameters which characterize the controlled system behavior. Then, given a fixed selection of  $\xi \in \Xi$ , periodic orbits can be found by numerically searching for fixed points of the following Poincaré return map  $\mathbf{P} : \mathcal{P} \times \Xi \rightarrow \mathcal{P}$  defined by

$$\mathbf{P}(\mathbf{x}_0, \xi) := \mathbf{x}(T^+; \mathbf{x}_0, \xi) \quad (21)$$

A large number of fixed points  $\mathbf{x}^* \in \mathcal{P}$  with  $\mathbf{x}^* = \mathbf{P}(\mathbf{x}^*, \xi)$  have been computed for  $v_d \in [3, 6.5]$  m/s and  $\alpha_\tau \in [0, 200]$  N m using MATLAB's `lsqnonlin` function to solve the nonlinear least-squares problem

$$\min_{\mathbf{x}} \|\mathbf{x} - \mathbf{P}(\mathbf{x}, \xi)\|^2 \quad (22)$$

with  $\mathbf{P}(\mathbf{x}, \xi)$  evaluated through forward simulation. For this simple model, fixed points are guaranteed to exist, as shown in Proposition 1. Figure 5 shows obtained periodic orbits for  $v \in \{3.0, 4.0, 5.0, 6.0\}$  m/s and  $\alpha_\tau \in \{0, 50, 100, 150\}$  Nm.

From Figure 5, it is shown that each fixed selection of  $\alpha_\tau$  results in lower peak-to-peak pitch amplitude as the speed increases. In order to maintain a more consistent peak-to-peak pitch amplitude over speed,  $\alpha_\tau$  is scaled proportionally to the vertical force magnitude  $\alpha_z$ . This is accomplished by scaling  $\alpha_\tau$  with  $\alpha_z$ , which relates  $\alpha_\tau$  to the gait timing through

$$\alpha_\tau = \tilde{\alpha}_\tau \frac{\tilde{T}_{st} T}{T_{st} \tilde{T}} \quad (23)$$

where tilde values represent fixed selections for a nominal speed of 3 m/s. Figure 6 shows the results across speed with this scaling for  $\alpha_\tau$  over various selections for  $\tilde{\alpha}_\tau$ .

When  $\tilde{\alpha}_\tau = 0$ , all ground reaction forces intersect the CoM, which may not be possible given the limitations of friction. In practice, the magnitude  $\tilde{\alpha}_\tau$  was chosen so that the body pitch angle  $\theta$  does not oscillate more than  $12^\circ$  for all speeds  $0 - 6.5$  m/s. A value of  $\tilde{\alpha}_\tau = 100$  N m met these requirements over all velocities  $v_d \in [3, 6.5]$  m/s and resulted in a minimum allowable friction coefficient of  $\mu = 0.56$ . This scaling law given by equation (23) represents one of many possible selections. More complex modulation of  $\alpha_\tau$  could be sought to manage the tradeoffs presented in Remark 5.

Linearizing  $\mathbf{P}$  about a fixed point  $\mathbf{x}^*$  results in a discrete-time linear system for the approximate dynamics of local perturbations around the orbit

$$\delta \mathbf{x}[i + 1] = \Psi \delta \mathbf{x}[i] \quad (24)$$

where  $\delta \mathbf{x} = \mathbf{x} - \mathbf{x}^*$

$$\Psi = \frac{\partial \mathbf{P}}{\partial \mathbf{x}}(\mathbf{x}^*, \xi) \quad (25)$$

If all eigenvalues of  $\Psi$  are strictly within the unit circle, local perturbations around the orbit will diminish over time (Nersesov et al., 2002). In contrast, the existence of an eigenvalue with an absolute value beyond the unit cycle precludes orbital stability (Nersesov et al., 2002). Numerically evaluating the eigenvalues of the matrix  $\Psi$  for  $v_d \in [3, 6.5]$  m/s and  $\alpha_\tau \in [0, 200]$  Nm verified that the obtained periodic orbits are unstable, as proved in general by Corollary 1.

#### 5. Gait stabilization

The impulse-based force profiles from the previous section scale across speeds and are guaranteed to give rise to periodic orbits. The instability of these orbits, however, motivates the development of gait stabilization control components. This section describes the addition of body-state feedback and a gait pattern stabilizer in order to admit new periodic orbits which enjoy asymptotic orbital stability. These additional controllers are layered on top of the

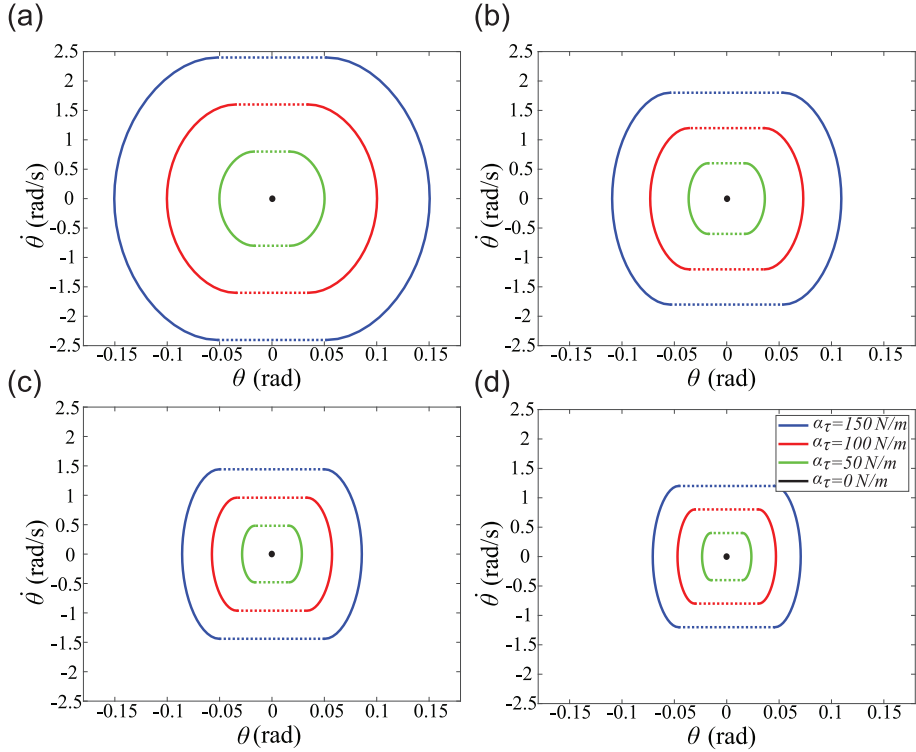


**Fig. 5.** Phase plot of the body pitch angle  $\theta$  for the periodic orbit for various values of  $v$  and  $\alpha_\tau$ . Dotted lines represent airborne durations, and solid lines represent stance durations. Top left:  $v = 3.0 \text{ m/s}$ , top right:  $v = 4.0 \text{ m/s}$ , bottom left:  $v = 5.0 \text{ m/s}$ , bottom right:  $v = 6.0 \text{ m/s}$ .

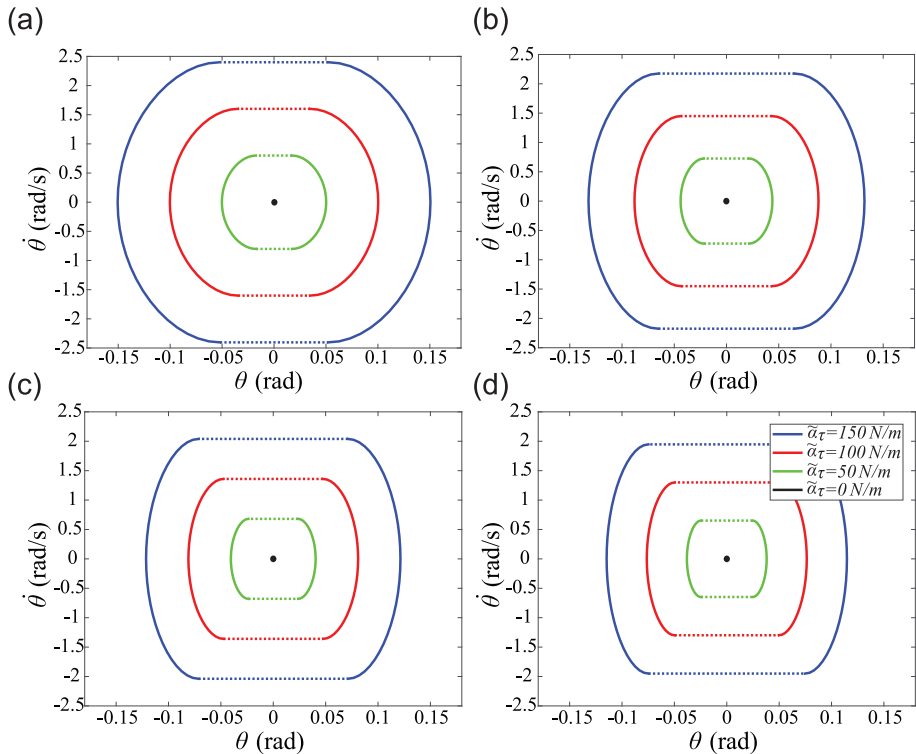


**Fig. 6.** Pitch limit cycles across speeds for different selections of  $\tilde{\alpha}_\tau$ . At each speed, values for the pitch magnitude  $\alpha_\tau$  are selected from the scaling law given by equation (23). Dotted lines represent airborne durations, and solid lines represent stance durations. Top left:  $v = 3.0 \text{ m/s}$ , bottom left:  $v = 4.0 \text{ m/s}$ , top right:  $v = 5.0 \text{ m/s}$ , bottom right:  $v = 6.0 \text{ m/s}$ .

impulse-based force planning and continue to be developed for simple planar models. Their implementation with experimental hardware is further detailed in Section 6.

### 5.1. Continuous body-state feedback

To stabilize the gait, additional feedback forces are considered beyond the impulse-based forces from the previous section. Forces  $\mathbf{F}$  are selected to include an impulse-based feedforward  $\mathbf{F}^*$  with three other components layered on top:

- vertical hip position feedback  $\mathbf{F}_{\text{Hip}}$ ;
- horizontal speed feedback  $\mathbf{F}_v$ ;
- pitch feedback  $\mathbf{F}_\theta$

$$\mathbf{F} = \mathbf{F}^* + \mathbf{F}_{\text{Hip}} + \mathbf{F}_v + \mathbf{F}_\theta \quad (26)$$

The feedforward forces provide nominal profiles, again parameterized by  $\alpha_\tau$  and  $\alpha_z$  as

$$\mathbf{F}^* := \begin{bmatrix} \frac{1}{z}(\tau^*(\alpha_\tau, s_{\text{st}}) + x F_z^*(\alpha_z, s_{\text{st}})) \\ F_z^*(\alpha_z, s_{\text{st}}) \end{bmatrix} \quad (27)$$

where  $F_z^*$  and  $\tau^*$  are given by equations (11) and (17) respectively.

The three feedback components are defined through impedance-based control laws

$$\mathbf{F}_{\text{Hip}} := \begin{bmatrix} 0 \\ g_{fb}(s_{\text{st}}) \left( -k_z^P(z_{\text{Hip}}^i - z_d) - k_z^D \dot{z}_{\text{Hip}}^i \right) \end{bmatrix} \quad (28)$$

$$\mathbf{F}_v := \begin{bmatrix} -k_x^D(\dot{x} - v_d) \\ 0 \end{bmatrix} \quad (29)$$

$$\mathbf{F}_\theta := \frac{1}{x} \begin{bmatrix} 0 \\ k_\theta^P(\theta - \theta_d) + k_\theta^D \dot{\theta} \end{bmatrix} \quad (30)$$

where,  $z_{\text{Hip}}^i \in \mathbb{R}$  is the hip height for  $i \in \{f, b\}$ . The feedback-activation function  $g_{fb}(s_{\text{st}})$  in equation (28) is a piecewise Bézier polynomial function that starts at zero and increases to 1.0 until 20% of the stance phase is complete. It then remains constant at 1.0 until 80% of the stance phase completes, and decreases to 0 when the stance terminates. Bézier coefficients of [0, 1, 1, 1] and [1, 1, 1, 0] are used to provide a smooth activation and deactivation of feedback in these periods of transition. This feedback-activation approach ensures that the total vertical direction force does not become negative near either end of the stance when  $F_z^* = 0$ . The  $1/x$  term in equation (30) takes into account the moment arm of the vertical direction force from the CoM. Prior to application in simulation, the resultant forces  $F_x$  from equation (26) are clamped based on a maximal assumed coefficient of friction  $\mu = 0.7$ .

**Remark 6.** Time-dependent trajectories for  $z_d(t)$ ,  $\theta_d(t)$ , and  $v_d(t)$  could be constructed from open-loop periodic limit cycles, resulting in different desired trajectories with

**Table 1.** Fixed parameter values for the simple hybrid model with feedback. Results for varying  $k_z^P$  with these parameters are given in Figure 7. Experiments of the MIT Cheetah were performed using  $k_z^P = 800$  N/m.

Parameter	Nominal value
$\alpha_\tau$	100 N m
$\theta_d$	0
$z_d$	0.48 m
$k_x^D$	60 N s/m
$k_z^D$	120 N s/m
$k_z^P$	30 N m/rad
$k_\theta^D$	15 N m/rad/s

changes in speed. However, the main focus here is to obtain robust bounding for various speeds rather than to follow exact trajectories. Thus, a fixed desired set point was used for  $\theta_d$  and  $z_d$  across speeds, while  $v_d$  was set to match the nominal commanded speed. These fixed selections serve as spring and damper setpoints that bias the motion toward desired states through stabilizing feedback.

**5.1.1. Stability analysis.** Through this addition of feedback, the parameter set is expanded such that  $\xi \in \Xi$  is defined with

$$\xi := (v_d, \alpha_\tau, \theta_d, z_d, k_x^D, k_z^P, k_z^D, k_\theta^P, k_\theta^D) \quad (31)$$

Many of these parameters were fixed from preliminary experimentation in hardware and are given in Table 1. For instance, damping coefficients were selected as the maximum values possible before the hardware becomes unstable due to noise caused from numerical differentiation of the encoder signals. Figure 7 shows the stability results on the spectral radius of the Monodromy matrix (Hiskens, 2001; Hiskens and Pai, 2000; Parker and Chua, 1989),  $\rho(\Psi)$ , for a range of fixed points that were computed with speeds  $v_d \in [3, 6.5]$  m/s and gains  $k_z^P \in [0, 2000]$  N/m. Over a large set of parameters, this additional feedback gives rise to orbitally stable dynamics for the time-based simple model.

### 5.2. A gait pattern stabilizer to enforce temporal footfall sequencing

In the simple model from Section 2, we assumed that the transition between phases occurred on a fixed timing schedule. Thus, this simple model effectively assumes perfect footfall timing. However, in the real robot this is not the case, as transitions from the aerial to stance phase occur when a swing leg touches the ground. As a result, footfall timing may be disturbed by swing leg movement and/or the body state in flight. This subsection presents a discrete controller to address these effects and an extended model to quantify pattern stabilization in simulation.

The trajectory for the swing foot's position relative to the hip is calculated using a Bézier curve with coefficients

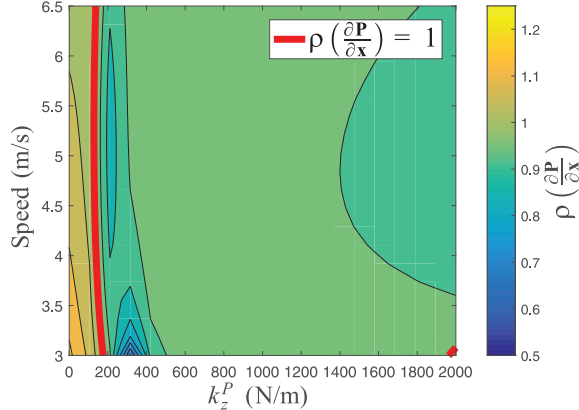


**Fig. 7.** Largest eigenvalues norms for  $\Psi = \frac{\partial \mathbf{P}}{\partial \mathbf{x}}$  at fixed points of  $\mathbf{P}$  over variations in  $v_d$  and  $k_z^P$ .

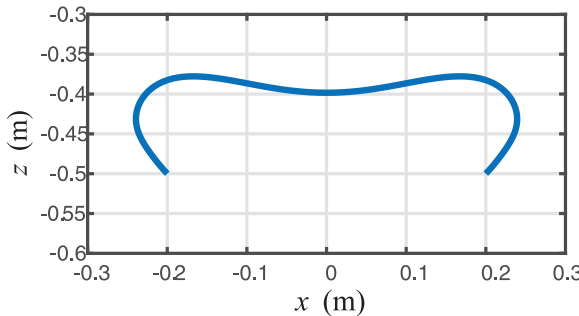


**Fig. 8.** Swing foot trajectory with respect to the hip during its aerial period of motion.

$\beta_x^{\text{sw}} \in \mathbb{R}^{10}$  and  $\beta_z^{\text{sw}} \in \mathbb{R}^{10}$  as obtained in the work by Park and Kim (2015)

$$x_{\text{foot}}^{i,d} := x_{\text{foot}}^{i,d}(\beta_x^{\text{sw}}, s_i) \quad (32)$$

$$z_{\text{foot}}^{i,d} := z_{\text{foot}}^{i,d}(\beta_z^{\text{sw}}, s_i), \quad s_i = \frac{t_{\text{sw}}^i}{T_{\text{sw}}} \quad (33)$$

where,  $t_{\text{sw}}^i \in \mathbb{R}_+$  represents the duration of time that leg  $i$  has been in flight and  $s_i \in \mathbb{R}_+$  is a phase variable indicating the percentage of the swing phase completed. Figure 8 shows the swing foot trajectories relative to the hip. Bézier parameters are set as given in Appendix 5.

**5.2.1. Gait pattern stabilizer.** Considering these swing trajectories, the desired symmetric gait pattern of bounding can be disrupted from step to step due to improperly timed impact events for the swing foot with the ground. Figure 9 illustrates this effect.

In order to enforce the desired temporal evolution of footfalls, a simple gait pattern stabilizer is introduced. The main idea is to adjust the duration of the stance phase to compensate for footfalls which are spaced too closely together or too far apart in time. A compensation gain  $\kappa \in [0, 1]$  is proposed to approximately specify how much error will be corrected in the current step. At each impact, a modified

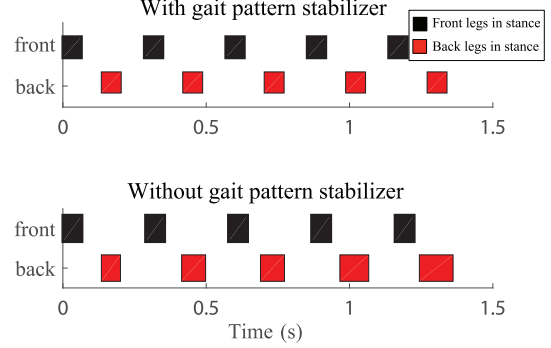


**Fig. 9.** Temporal gait shifting with gait pattern stabilizer (top), and without gait pattern stabilizer (bottom) during 6 m/s running. Shaded regions indicate periods of stance.

stance time for the next foot is updated as

$$T_{\text{st}}^+ = \frac{L}{v_d} - \kappa (T_{\text{st}}^- + \bar{t}^- - T/2) \quad (34)$$

The term  $T_{\text{st}}^-$  is the stance time for the previous foot and  $\bar{t}^-$  is the most recent aerial time. Thus,  $T_{\text{st}}^- + \bar{t}^-$  measures the time since the previous impact and  $T_{\text{st}}^- + \bar{t}^- - T/2$  represents the gait timing error from a symmetric footfall pattern. If each following footfall happens at the end of the nominal swing time, it can be shown that this control law provides asymptotic tracking to the desired gait pattern, and is applicable more broadly to other footfall sequences as described in the following proposition.

**Proposition 2.** (*Asymptotic stability of the gait pattern stabilizer under nominal conditions*). For an  $N$  beat gait, let  $T_{\text{st}}^i[k]$  represent the stance duration for foot  $i$  following its  $k$ -th footfall,  $T_{\text{st}}^{i*}$  the nominal stance time, and  $e_i[k]$  the error in footfall timing between foot  $i$  and its predecessor. Suppose that each subsequent swing period lasts  $T_{\text{sw}}^i = T - T_{\text{st}}^{i*}$  and stance durations are updated as

$$T_{\text{st}}^i[k] = T_{\text{st}}^{i*} - \kappa e_i[k]$$

for some  $\kappa \in (0, 1)$ . Then following any initial gait timing errors  $e_i[0]$ , the footfall timing errors satisfy  $e_i[k] \rightarrow 0$  as  $k \rightarrow \infty$ .

*Proof.* The proof is given in Appendix 6.  $\square$

Proposition 2 assumes that each following footfall happens at the end of the nominal swing time, but this is not guaranteed when the gait pattern stabilizer is actually applied to the system with drift vector fields and impact events. Therefore, an extended hybrid model, described in the following paragraphs, is introduced to demonstrate the existence of asymptotically stable footfall timing when this gait pattern stabilizer is layered on top of the impulse-based controller with the body-state feedback designed so far.

### 5.3. An extended model for gait pattern stability analysis

In order to check the stability of the full hybrid feedback system with the gait pattern stabilizer given by equation (34), auxiliary variables are added to the simple hybrid bounding model from Section 2. Phase variables  $s_f$  and  $s_b$  are added for swing foot trajectories defined in equation (33) and the stance time  $T_{st}$  is included to capture the effects of the pattern stabilizer. The extended state  $\mathbf{x} := (\mathbf{q}, \dot{\mathbf{q}}, \bar{t}, s_f, s_b, T_{st})$  is applicable across phases.

In this extended model, stance phases end when the stance time is reached. The transition out of stance affects only the phase time and swing phase variables

$$\mathcal{S}_1 = \mathcal{S}_3 := \{\mathbf{x} \text{ s.t. } \bar{t} - T_{st} = 0\} \quad (35)$$

$$\Delta_1(\mathbf{x}) := (\mathbf{q}, \dot{\mathbf{q}}, 0, 0, s_b, T_{st}) \quad (36)$$

$$\Delta_3(\mathbf{x}) := (\mathbf{q}, \dot{\mathbf{q}}, 0, s_f, 0, T_{st}) \quad (37)$$

Flight phases end when the swing foot touches the ground. It is noted that the position of the body relative to the swing foot, denoted  $(x_{sw}^i, z_{sw}^i)$  for  $i \in \{f, b\}$  can be specified through the phase  $s_i$  and pitch angle  $\theta$  directly. Thus, transitions occur at

$$\mathcal{S}_2 := \{\mathbf{x} \text{ s.t. } z_{sw}^b(\theta, s_b) - z = 0\} \quad (38)$$

$$\mathcal{S}_4 := \{\mathbf{x} \text{ s.t. } z_{sw}^f(\theta, s_f) - z = 0\} \quad (39)$$

Following this definition, it is observed that all guards  $\mathcal{S}_j$  can be defined such that they are the kernel of an appropriately chosen function  $\mathbf{s}_j : \mathcal{D}_j \rightarrow \mathbb{R}$ .

Following impact, the model transitions to a state with an updated body position  $x$ , which reflects the coordinate origin of the new stance foot. As a result,  $\Delta_2(\mathbf{x})$  and  $\Delta_4(\mathbf{x})$  are given as

$$\begin{aligned} \Delta_2(\mathbf{x}) &:= [x_{sw}^b(\theta, s_b) \ z \ \theta \ \dot{\mathbf{q}}^T \ 0 \ s_f \ s_b \ T_{st}^+]^T \\ \Delta_4(\mathbf{x}) &:= [x_{sw}^f(\theta, s_f) \ z \ \theta \ \dot{\mathbf{q}}^T \ 0 \ s_f \ s_b \ T_{st}^+]^T \end{aligned}$$

respectively where  $T_{st}^+$  follows equation (34). The 0 after  $\dot{\mathbf{q}}$  in each reset map sets the dwell time to zero whenever a transition happens.

In the extended model, the system dynamics given by equation (4) are changed to depend on the gait phase

$$\mathbf{f}_1 = \begin{bmatrix} \mathbf{f} \\ 1/T_{sw} \\ 0 \\ 0 \end{bmatrix}, \mathbf{f}_3 = \begin{bmatrix} \mathbf{f} \\ 0 \\ 1/T_{sw} \\ 0 \end{bmatrix}, \mathbf{f}_2 = \mathbf{f}_4 = \begin{bmatrix} \mathbf{f} \\ 1/T_{sw} \\ 1/T_{sw} \\ 0 \end{bmatrix} \quad (40)$$

and

$$\mathbf{g}_1 = \dots = \mathbf{g}_4 = \begin{bmatrix} \mathbf{g} \\ 0_{3 \times 1} \end{bmatrix} \quad (41)$$

where, the elements with  $1/T_{sw}$  come from  $s_i = t_{sw}^i/T_{sw}$  in equation (33).

#### 5.3.1. Investigating periodic orbits with gait pattern stabilization.

The inclusion of the gait pattern stabilizer adds a single additional parameter  $\kappa$  to the parameter vector  $\xi$

$$\xi := (v_d, \alpha_t, \theta_d, z_d, k_x^D, k_z^P, k_z^D, k_\theta^P, k_\theta^D, \kappa) \quad (42)$$

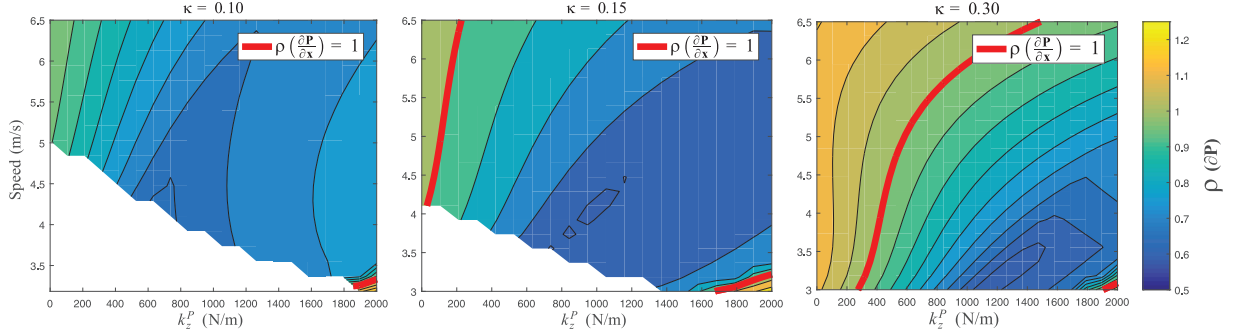
With this addition, new fixed points  $\mathbf{x}^*$  were found for the return map  $\mathbf{P}(\mathbf{x}, \xi)$ . First-order sensitivity information along the orbit associated with each fixed point was derived through computation of the Monodromy matrix (Hiskens, 2001; Hiskens and Pai, 2000; Parker and Chua, 1989).

Figure 10 shows the spectral radius of  $\Psi$ ,  $\rho(\Psi)$ , with three different selections of  $\kappa$  and over a range of speed and gain values. As shown in the figure, smaller values of  $\kappa$  pose parameter regions where fixed points do not exist. These regions occur at low speeds and correspondingly have a higher duty factor with less flight time. In these cases, without strong gait pattern stabilization, the system tends towards bounding gaits with periods of double support that are not captured in the current hybrid model. This effect is shown in the bottom of Figure 9 for the extreme case of no pattern stabilization ( $\kappa = 0$ ). Experimental validation of the algorithm is performed using  $\kappa = 0.3$  and  $k_z^P = 800$  N/m. While periods of double support are not captured in the event-driven simple bounding model, the following section provides further details on an experimental application of the algorithm which is flexible to handle these scenarios. The analysis of gaits which may switch mode sequences is beyond the scope of the current analysis.

## 6. Controller implementation details

The impulse-based force profiles from Section 4 and layered feedback from Section 5 gives rise to asymptotically stable periodic orbits for the event-driven simple bounding model. This simple model is an appropriate abstraction for the MIT Cheetah robot in bounding. However, the experimental hardware is not constrained to the plane and has light legs which do require careful treatment in order to realize the foot-force centered controllers developed in the previous section. This section presents the implementation details to realize the control design on the real robot hardware.

Figure 11 shows the overall control system for the Cheetah robot, with many of the control system blocks detailed further in this section. The MIT Cheetah 2 has 3D kinematics which extend beyond those captured in the planar simple model. As shown in Figure 12(a), each leg of the MIT Cheetah 2 consists of three links beginning from the shoulder joint. The motions of the first and last link from the shoulder are kinematically tied to be parallel to each other, resulting in two degrees of freedom in the leg swing plane. The first actuator torque  $u_{sh}$ , rotates the link represented by the thick solid black line in Figure 12(a), providing rotation of all three links relative to the body. The second actuator torque  $u_{kn}$  rotates the link represented by the dashed red line, yielding rotation of the second link while the first and



**Fig. 10.** Largest eigenvalue norms of the Poincaré return map linearization for the extended bounding model with different values of  $\kappa$ . White areas indicate regions where a fixed point was not found to exist for the hybrid mode schedule considered in this work.

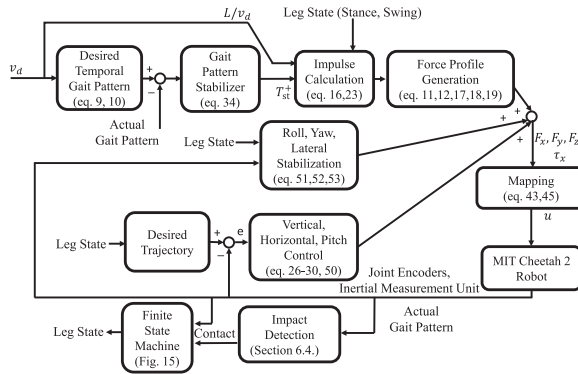


**Fig. 11.** Overall control system diagram.

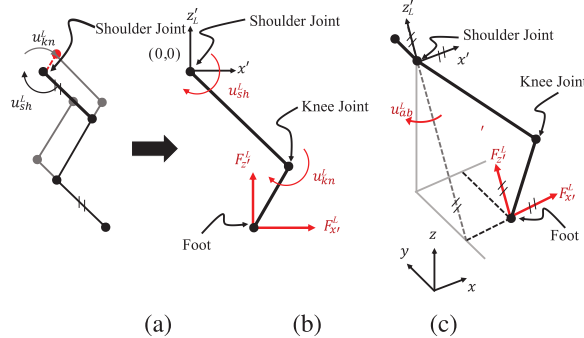


**Fig. 12.** (a) MIT Cheetah's leg consisting of three links. The first and third links are kept in parallel to each other by the parallelogram mechanism. (b) Two link kinematic conversion of original link structure. Using the torques  $u_{sh}$  and  $u_{kn}$  at the shoulder and knee joints, forces  $F_{x'}$  and  $F_{z'}$  are generated. (c) An additional actuator creates ab/adduction torque  $u_{ab}$  for each leg.

third links are kept in parallel. Because the first and third links are parallel, the original link structure can be kinematically converted to a mechanism with only two links shown in Figure 12(b). In addition to the actuators for the knee and shoulder angles, there is one more actuator to create ab/adduction torque  $u_{ab}$  for each leg (see Figure 12(c)).

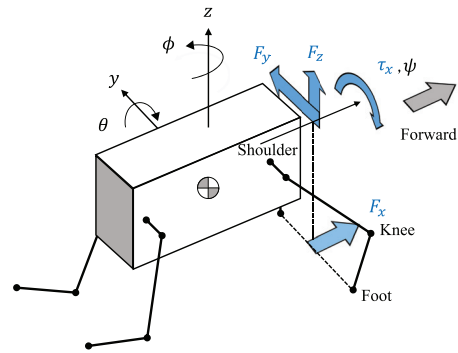


**Fig. 13.** Coordinates system and control forces of MIT Cheetah 2.  $\psi$ ,  $\theta$ , and  $\phi$  are roll, pitch, and yaw angles representing rotations about  $x$ -,  $y$ -, and  $z$ -axis, respectively. The horizontal force  $F_x$ , lateral force  $F_y$ , vertical force  $F_z$ , and rolling torque  $\tau_x$  are generated using actuator torques of each pair of the legs (see Figures 12 and 14).

### 6.1. Specification of leg forces and joint torques for 3D bounding

To realize the force profiles from the simple model controller using available actuators, this subsection presents a solution to the static force-production problem. More specifically, we obtain a relationship based on kinematics only, which is used to realize horizontal, lateral, and vertical forces, as well as a net rolling torque ( $F_x, F_y, F_z$ , and  $\tau_x$  in Figure 13) through available actuators. Solution of this problem is used to stabilize the posture during 3D bounding.

This force-production problem is closely linked to closed-chain-constrained operational-space control of body posture (Hutter et al., 2014b; Sentis et al., 2010; Wensing et al., 2015). The procedure used here approximates these previous approaches through assuming massless legs, and symmetry in the production of fore-aft force. This former approximation is reasonable, as the robot's legs are relatively light compared to the body (less than 10% of the total mass). The procedure for solving the force-production problem is two-fold and is depicted in Figure 14.

**6.1.1. Reduction to a frontal-plane force-production problem.** In the first step, an auxiliary coordinate system and a force-symmetry assumption are used to reduce the 3D force-production problem to one in the frontal plane. An auxiliary planar coordinate system  $x'z'_L$  rotated from the  $xz$  coordinate system by ab/adduction angle  $q_{ab}^L$  is attached on the shoulder joint (see Figure 14(a)). In this planar coordinate system, we can obtain a mapping from the forces  $F_{x'}^L$  and  $F_{z'}^L$  at the left foot, shown in Figure 14, to the torques  $u_{sh}^L$  and  $u_{kn}^L$  which is given by,

$$\begin{bmatrix} u_{sh}^L \\ u_{kn}^L \end{bmatrix} = \mathbf{J}_{x'z'_L}^T \begin{bmatrix} F_{x'}^L \\ F_{z'}^L \end{bmatrix} \quad (43)$$

where,  $\mathbf{J}_{x'z'_L} \in \mathbb{R}^{2 \times 2}$  is the manipulator Jacobian obtained by taking the partial derivative of the position of the foot relative to the shoulder in the  $x'z'_L$  coordinates with respect to the knee and shoulder joint angles. For the right leg, the same procedure is followed. Then, the horizontal force  $F_x$  is just the summation of the left and right horizontal forces  $F_{x'}^L$  and  $F_{x'}^R$  as shown in Figure 14(a). In order to avoid unnecessary yaw torque,  $F_{x'}^L$  and  $F_{x'}^R$  are chosen to be the same, thereby obtaining

$$F_{x'}^L = F_{x'}^R = \frac{1}{2}F_x \quad (44)$$

**6.1.2. Solution of the frontal-plane force-production problem.** In the second step, we design a linear operator  $\Pi \in \mathbb{R}^{4 \times 3}$  which produces the desired net force/torque vector  $\mathbf{F}_B := (F_y \ F_z \ \tau_x)^T$  on the floating base in the frontal plane through a set of leg forces  $\mathbf{u}_{\text{frt}} = (F_{z'}^L \ F_{z'}^R \ u_{ab}^L \ u_{ab}^R)^T$  (see Figure 14(b)) as

$$\mathbf{u}_{\text{frt}} = \Pi \mathbf{F}_B \quad (45)$$

The mapping  $\Pi$  is designed such that the leg forces result in the correct net force on the floating base when considering the effect of the closed-chain kinematic constraints of the legs with the ground. To systematically obtain the mapping, we define generalized coordinates of the floating base frontal dynamics as

$$\mathbf{q}_{\text{frt}} := [\mathbf{q}_B^T \ \mathbf{q}_\ell^T]^T \in \mathbb{R}^{7 \times 1} \quad (46)$$

where, body DoFs  $\mathbf{q}_B = [y_B, z_B, \psi]^T$  and leg DoFs  $\mathbf{q}_\ell = [z_L, z_R, q_{ab}^L, q_{ab}^R]^T$ . Variables  $y_B$  and  $z_B$  provide the position of the body in the frontal plane,  $\psi$  is the roll angle,  $z_L$  and  $z_R$  are the length of the left and right legs in frontal plane, and  $q_{ab}^L$  and  $q_{ab}^R$  are ab/adduction angles of left and right legs (see Figure 14(b)).

To take into account the constraints of ground contact, let  $\mathbf{p}_{\text{foot}} \in \mathbb{R}^{4 \times 1}$  be the vector which has the elements of the horizontal and vertical foot position of the left and right legs in the frontal plane. Then, the constraints can be written as

$$\dot{\mathbf{p}}_{\text{foot}} = \mathbf{J}_{\text{foot}} \dot{\mathbf{q}}_{\text{frt}} \equiv 0 \quad (47)$$

$$\ddot{\mathbf{p}}_{\text{foot}} = \mathbf{J}_{\text{foot}} \ddot{\mathbf{q}}_{\text{frt}} + \mathbf{J}_{\text{foot}} \dot{\mathbf{q}}_{\text{frt}} \equiv 0 \quad (48)$$

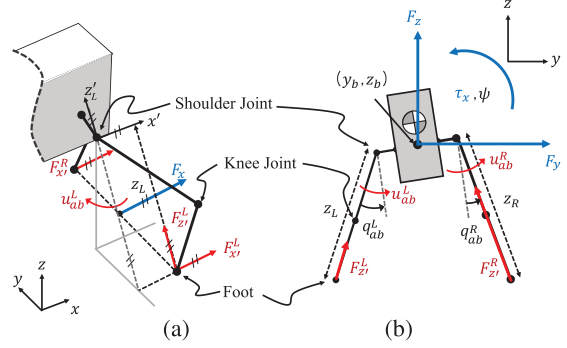


**Fig. 14.** Generation of the lateral force  $F_y$ , vertical force  $F_z$ , and rolling torque  $\tau_x$  using forces  $F_{z'}^L$  and  $F_{z'}^R$ , and torques  $u_{ab}^L$  and  $u_{ab}^R$  for two legs contacting with the ground.  $y_B$  and  $z_B$  are the position of the center of the left and right shoulder joints in frontal plane,  $\psi$  is the rolling angle of the body, and  $q_{ab}^L, q_{ab}^R$  are ab/adduction angles of the left and right legs.

To aid the following development, the foot Jacobian  $\mathbf{J}_{\text{foot}}$  is partitioned as

$$\mathbf{J}_{\text{foot}} = [\mathbf{J}_B \ \mathbf{J}_\ell]$$

Derivation of the constrained dynamics of the planar mechanism reveals how the actuation  $\mathbf{u}_{\text{frt}}$  affects the body dynamics. Letting  $\mathbf{I}_B = \text{diag}(m, m, I_\phi)$ , the spatial inertia tensor for the body in the frontal plane, and approximating legs as massless, the dynamics of this planar frontal system are given through

$$\begin{bmatrix} \mathbf{I}_B & 0 & -\mathbf{J}_B^T \\ 0 & 0 & -\mathbf{J}_\ell^T \\ \mathbf{J}_B & \mathbf{J}_\ell & 0 \end{bmatrix} \begin{bmatrix} \ddot{\mathbf{q}}_B \\ \ddot{\mathbf{q}}_\ell \\ \lambda \end{bmatrix} = \begin{bmatrix} 0 \\ \mathbf{u}_{\text{frt}} \\ -\mathbf{J}_{\text{foot}} \dot{\mathbf{q}}_{\text{frt}} \end{bmatrix}$$

where  $\lambda$  is a Lagrange multiplier associated with the constraint. The three zeros in the upper-left block of the mass matrix are due to the assumption of massless legs. From the second row,  $-\mathbf{J}_\ell^T \lambda = \mathbf{u}_{\text{frt}}$ , and it follows that the body dynamics are given as

$$\mathbf{I}_B \ddot{\mathbf{q}}_B = -\mathbf{J}_B^T \mathbf{J}_\ell^{-T} \mathbf{u}_{\text{frt}}$$

Further,  $\mathbf{J}_\ell$  is guaranteed invertible by the choice of coordinates. In order to impart the desired body force  $\mathbf{F}_B$ , we seek

$$-\mathbf{J}_B^T \mathbf{J}_\ell^{-T} \mathbf{u}_{\text{frt}} = \mathbf{F}_B \quad (49)$$

Thus, as one of many possible solutions,  $\Pi$  is selected as  $\Pi = -(\mathbf{J}_B^T \mathbf{J}_\ell^{-T})^\dagger$  where  $(\cdot)^\dagger$  provides the Moore-Penrose pseudoinverse.

**Remark 7.** It is interesting to note that the quantity  $-\mathbf{J}_B^T \mathbf{J}_\ell^{-T}$  maps leg actuations to effective forces on the floating base under considerations of contact. Thus, it plays an analogous role to the transpose of the dynamically-consistent Jacobian pseudoinverse associated with a floating-base postural task in closed-chain-constrained operational-space control (Sentis et al., 2010;

Wensing et al., 2015). However, the legs are assumed massless in this current model, resulting in a static mapping (i.e. one that is a function of kinematic parameters alone). This result is in contrast to the required inversion of the mass matrix in other task-space methods which include leg mass (Hutter et al., 2014b; Wensing et al., 2015).

**Remark 8.** For the frontal plane system with massless legs, the problem of floating-base task-space control is equivalent to floating-base inverse dynamics. As a result, the above development may be seen as a special case of previous methods (Mistry et al., 2010; Righetti et al., 2011, 2013). The previous remark, concerning the benefit of not requiring a mass matrix inversion, can be interpreted to flow from the benefits of these more general approaches. It is important to note, however, that even with massless legs the full 3D force-production problem cannot be cast as one of floating-base inverse dynamics, since 3D bounding is underactuated.

**6.1.3. Use of the 3D force-production solution for postural stabilization.** This solution to the 3D force production problem is combined with the 2D force profiles and feedback from Section 5.1 as well as additional out-of-plane forces to stabilize bounding in 3D. The forces  $F_x$  and  $F_z$  are selected as

$$\begin{bmatrix} F_x \\ F_z \end{bmatrix} = \mathbf{F} + \begin{bmatrix} -k_x^P(x - x_d(t)) \\ 0 \end{bmatrix} \quad (50)$$

where,  $\mathbf{F}$  is from equation (26),  $x_d(t)$  is a desired horizontal motion with velocity fixed at the desired speed  $\dot{x}_d(t) = v_d$  (reset each step), and  $k_x^P$  is chosen as 1500 N/m. To regulate the lateral sway and rolling motion of the body,  $F_y$  and  $\tau_x$  are chosen as

$$F_y = -k_y^P y_B - k_y^D \dot{y}_B \text{ and} \quad (51)$$

$$\tau_x = -k_\psi^P \psi - k_\psi^D \dot{\psi} \quad (52)$$

To regulate yaw motion, the following feedback is calculated

$$F_{y,\phi}^i = \sigma (-k_\phi^P(\phi - \phi_d) - k_\phi^D \dot{\phi}) \quad (53)$$

where,  $\phi_d$  is the desired yaw angle, and  $\sigma = 1$  and  $-1$  for the front leg and hind leg. This feedback is added to the force  $F_y$  in equation (51). Following this specification of desired forces and torques  $F_x, F_y, F_z$ , and  $\tau_x$ , the joint torques  $u_{sh}^L, u_{sh}^R, u_{kn}^L, u_{kn}^R, u_{ab}^L$ , and  $u_{ab}^R$  are obtained using equations (43)–(45).

## 6.2. Swing foot trajectory tracking

In order to track the desired swing foot position in flight, a Cartesian impedance controller is employed nominally around the trajectory specified through equations (32) and (33). This subsection details a set of Beziér curve based

methods which provide online adaptation of the desired trajectory for experimental implementation.

Regardless of running speed, the nominal swing foot trajectories are based on the same set of Beziér coefficients. Two modifications to the Beziér trajectories are pursued to improve swing leg performance. First, it is important to touchdown with a ground-matched velocity as speed increases. This ground speed matching can occur through early retraction, and provides decreased impact losses. This is important to address as an implementation issue, as the leg mass was not previously captured in the simple models of the previous sections. Second, while tracking the nominal trajectory around the impact event is important, a smoother leg repositioning response can be obtained if tracking requirements are relaxed for the first half of swing.

**6.2.1. Phase warping for early retraction.** In order to achieve the desired retraction speed at the end of the swing, a third-order phase-warping Bézier polynomial  $s_{sw}(\beta_s^{sw}, s)$  is employed to provide

$$x_{foot}^d := x_{foot}^d(\beta_x^{sw}, s_{sw}(\beta_s^{sw}, s)) \quad (54)$$

with the following Bézier coefficients

$$\beta_s^{sw} = \begin{bmatrix} 0 \\ \frac{1}{3} (\dot{x}_{foot}^d(\beta_x^{sw}, 0))^{-1} \dot{x}_{foot}(\tau) \\ 1 - \frac{1}{3} (\dot{x}_{foot}^d(\beta_x^{sw}, 1))^{-1} v_d \\ 1 \end{bmatrix} \quad (55)$$

where,  $\tau$  is the time at the end of the stance phase.

It can be verified that this phase warping provides the following

$$\dot{x}_{foot}^d(0) = \left. \frac{\partial x_{foot}^d}{\partial s_{sw}} \dot{s}_{sw} \right|_{s=0} = \dot{x}_{foot}(\tau) \quad (56)$$

$$\dot{x}_{foot}^d(1) = \left. \frac{\partial x_{foot}^d}{\partial s_{sw}} \dot{s}_{sw} \right|_{s=1} = v_d \quad (57)$$

which matches the actual horizontal velocity at liftoff and desired horizontal velocity at touchdown.

**6.2.2. Correction polynomial for smooth early-flight tracking.** At the beginning of flight, the actual leg configuration may be far from the nominal swing trajectory, causing a high-jerk response from the flight-leg impedance control. To improve the smoothness of the closed-loop response, the desired trajectory is modified through the addition of a third-order Bézier polynomial  $h_x^{\text{corr}}(s_{\text{corr}}), h_z^{\text{corr}}(s_{\text{corr}})$  with the following characteristics

$$h_x^{\text{corr}}(0) = x_{foot}(\tau) - x_{foot}^d(0)$$

$$h_z^{\text{corr}}(0) = z_{foot}(\tau) - z_{foot}^d(0)$$

$$h_x^{\text{corr}}(1) = 0$$

$$h_z^{\text{corr}}(1) = 0$$

A zero rate-of-change was enforced at the beginning and end of this polynomial, which determines the polynomial uniquely. We call this polynomial a correction polynomial (Chevallereau et al., 2009), as it captures the tracking error at the beginning of flight and smoothly decays to zero. In order to ensure an accurate touchdown foot position, it is desired for any correction to decay to zero by 50% of the way through the swing phase. An effective approach is to specify  $s_{\text{corr}}$  as

$$s_{\text{corr}}(s_{\text{sw}}) := \begin{cases} 2s_{\text{sw}} & \text{if } s_{\text{corr}} \leq 1 \\ 1 & \text{o.w.} \end{cases} \quad (58)$$

Then, the online corrected swing foot trajectory becomes

$$\begin{aligned} x_{\text{foot}}^{\text{corr}} &= x_{\text{foot}}^d(\beta_x^{\text{sw}}, s_{\text{sw}}) + h_x^{\text{corr}}(s_{\text{corr}}(s_{\text{sw}})) \\ z_{\text{foot}}^{\text{corr}} &= z_{\text{foot}}^d(\beta_z^{\text{sw}}, s_{\text{sw}}) + h_z^{\text{corr}}(s_{\text{corr}}(s_{\text{sw}})) \end{aligned} \quad (59)$$

Note that this choice of swing foot trajectory does not provide matching on the vertical velocity  $z_{\text{foot}}$  at the start of the swing phase, but this is intentional. Rapid response to eliminate foot lift velocity errors is critical for consistent ground clearance.

### 6.3. Accounting for swing-leg effects in flight

In the experiments, the effects of swing leg inertia cause the robot to rotate clock-wise in pitch angle. To address this effect, the nominal force profiles are modified during the stance in experiments. More specifically, the force profiles in equation (12) employ a modified value of  $s_{\text{peak}} = 0.3$ . This value causes the peak vertical force to occur earlier in the stance, which has been found to correlate with a nose-up pitch in simulations. Thus, the effect of  $s_{\text{peak}}$  roughly compensates for the nose-down pitch from the swing-leg effects.

### 6.4. Impact detection

Impact with the ground is detected by proprioception, observing the force in the  $z$ -direction created by joint actuators. The required nominal  $z$ -direction inertial force to create the desired swing motion is logged from prior swing leg motion experiments during which the robot is hanging in the air. This data is used to create a table of phase-dependent inertial forces required for a leg swing. In the bounding experiment, if the  $z$ -direction force during the swing phase is larger than this phased-dependent inertial force by some margin, this additional force is assumed to be caused by the impact with the ground, and touchdown is declared. As a drawback, this approach may lead to a delay in the detection of the ground impact during bounding which acts as a persistent disturbance to the gait pattern stabilizer.

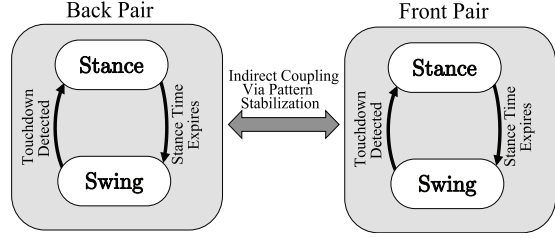


**Fig. 15.** In the hardware experiments, separate state machines are employed for each pair of legs. Coupling is provided indirectly through the dynamics of bounding and the gait pattern stabilizer.

### 6.5. Indirectly-coupled leg-dependent finite state machines

The last step of the implementation process is to introduce a state machine to manage transitions between the stance and swing phase for each leg. Two independent finite state machines for each pair of front and hind legs are proposed. That is, each state machine governs the transition of a pair of legs, left and right, which occur together. Timing synchronization between the front pair of legs and hind pair of legs is accomplished by indirect coupling through the gait pattern stabilizer alone. The state machine is illustrated in Figure 15. As in the simple hybrid bounding model, the transition from swing to stance occurs when the leg strikes the ground. The transition from stance to swing takes place when the leg leaves the ground. This approach is effective in experiments to handle periods of double support which are not captured in the simple hybrid models from the previous sections.

## 7. Experiments and results

This section documents the experimental results of the controller applied in the 3D bounding trials. The experiment starts with the robot standing on four legs until an operator initiates bounding. For the first step of each leg, a time-dependent open-loop force profile is applied as specified in Section 4. Once airborne, a finite state machine for each pair of legs is started. Feedback is applied in every stance phase thereafter. In order to apply the stance time specified in equation (9), an additional scaling parameter  $\gamma \in [0, 1]$  is introduced

$$\gamma := \min\left(\frac{v_d}{3 \text{ m/s}}, 1\right)$$

with the nominal stride length then set as

$$L = \gamma L^* \quad (60)$$

with  $L^* = 0.4 \text{ m}$ . The trajectory of the swing leg in the horizontal direction is similarly scaled by  $\gamma$  such that when  $\gamma = 1$ , the leg moves in a full horizontal stroke. The nominal trajectory of the leg in the vertical direction is not scaled by this parameter.

The experiment starts with  $v_d = 0$  and the desired speed increased from step to step as shown in Figure 16.

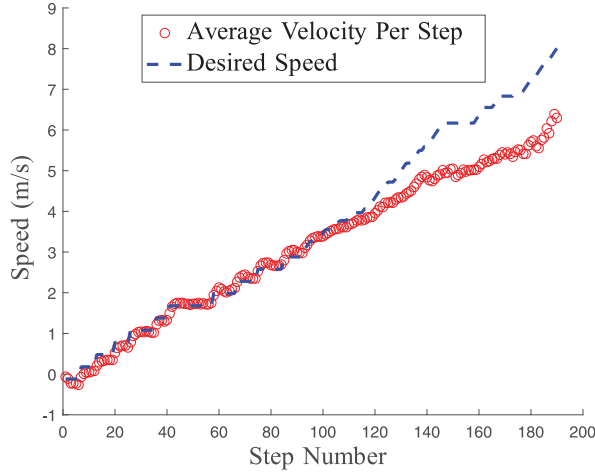


**Fig. 16.** Velocity tracking over time for max speed experiment. Actual velocity was estimated from the average speed of the stance hips relative to the feet. A video of the experiment is available in Extension 1.

The speed of the treadmill is adjusted by a human operator independently from the desired speed in order to prevent nonsmooth increases in the treadmill speed which may destabilize the robot. In the experiment, the MIT Cheetah 2 increases its speed from 0 m/s up to a max speed of 6.4 m/s when roll instability leads to the end of the run (see Extension 1). At lower speeds, the extension shows fully unconstrained 3D bounding. However, challenges in steering on a narrow treadmill at the highest speeds necessitated partial leaning against the side wall during portions of the gait phase. During the experiment, the minimum and maximum pitch for each stride stay within the range  $[-0.26 \text{ rad}, 0.13 \text{ rad}]$  as shown in Figure 17. Figure 18 shows the mean and standard deviation for the min and max pitch versus speed. Beyond 3.0 m/s, the controller uses the same nominal stride length within each step and exhibits less variability from the average pitch. For the binning shown in Figure 16, bins with speeds under 3.0 m/s have a mean standard deviation of 0.027 rad while bins above 3.0 m/s had a mean standard deviation of 0.014 m/s. While faster gaits are expected to have a smaller peak-to-peak magnitude at higher speeds due to the pitch moment scaling from equation (23), it is interesting that these faster speeds also have more consistent pitch performance in the hardware.

### 7.1. Gait pattern stabilization

Figure 19 shows the result of the stabilized gait pattern during the maximum speed experiment. Following an initial transient in the first three steps, the relative timing in between footfalls has a maximum error of 24.9% and an average error of 6.0% from the nominal timing. This shows the effectiveness of the gait pattern stabilizer to couple the otherwise independent state machines which drive the front and back legs in the experimental platform.

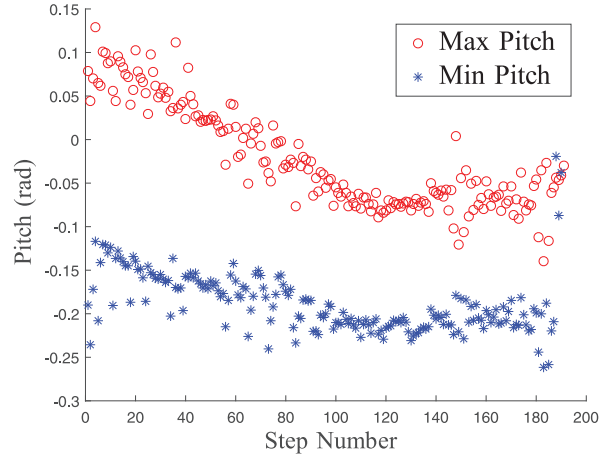


**Fig. 17.** Minimum and maximum pitch angle per step during the maximum speed experiment. Maximum pitch (nose down) occurs during front stance and minimum pitch occurs during back stance.

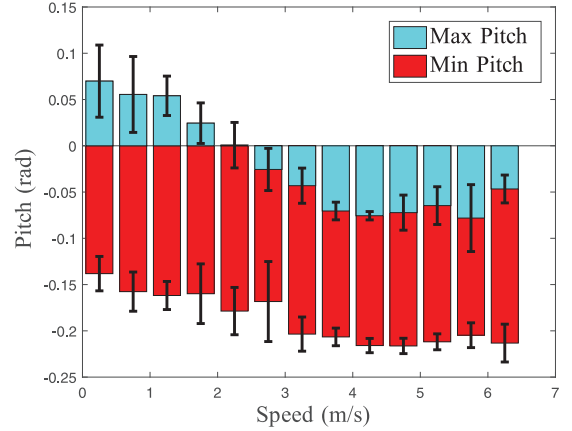


**Fig. 18.** First and second moments of the distribution over min/max pitch vs. speed. The height of the bars represent the average min/max pitch and the solid lines represent  $\pm$  one standard deviation.

### 7.2. Impulse scaling

The only changes to the controller parameters across the speed are those which are automatically computed using the principles of impulse scaling. Figures 20 and 21 show characteristic profiles for the desired forces when running at 2 m/s and 6 m/s respectively. The desired forces are computed through a leg Jacobian transpose from the torques commanded to the actuators. Torque commands for the shoulders and knees are shown in Figures 22 and 23. Only closed-loop joint torque control to these values was used to (approximately) render desired forces at the feet. The accuracy of this method for rendering desired forces is thus dependent on dynamic conditions which are not captured in the static mapping. Force-tracking results for this approach are quantified by Wensing et al. (2016).

Feedforward forces change significantly across speed and dominate the total desired forces. Feedforward vertical forces  $F_z^{f,b}$  (*ff*) have a maximum magnitude of 240 N when

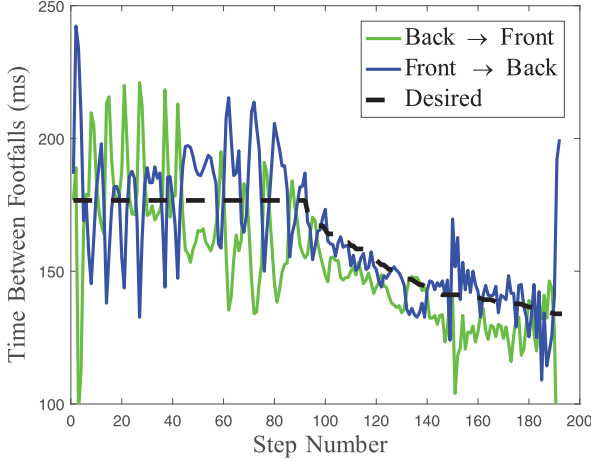


**Fig. 19.** Tracking desired gait pattern timing during the maximum speed experiment. As speed increases beyond 3 m/s, the stance time and overall period decrease.

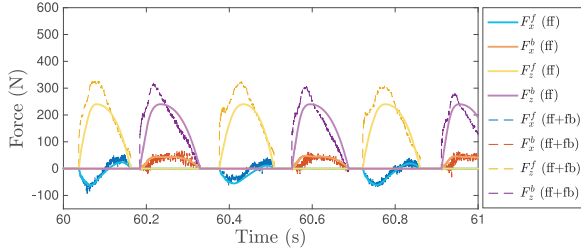


**Fig. 20.** Desired sagittal plane forces when running at 2 m/s. Solid lines indicate the feedforward forces from vertical momentum and pitch moment scaling. Dashed lines represent forces with feedback included.

running at 2 m/s, compared to 500 N when running at 6 m/s. It is observed that the feedforward force profile (solid) provides a majority of the total force (dashed) indicating the prominent role of the momentum-based nominal force in the closed-loop control. In fact, this feedforward force plays a relatively more important role at higher speeds. At 2 m/s, the vertical force deviates from the feedforward by an average of 49.5 N during stance, which is 20.6% of the peak force. At 6 m/s the desired vertical force deviates from the feedforward by an average of 63.3 N, only 12.7% of the peak force.

This dominant role of these feedforward forces is one of the main differences from previous work with Cheetah 1 (Hyun et al., 2014). In that work, the ground reaction forces were purely the result of interactions between leg impedances and the ground through high-gain foot position control. For comparison, the value of the vertical stiffness in prior work was 5000 N/m for each leg, or effectively 10,000 N/m in total with two legs on the ground. The total vertical stiffness in this current work is  $k_z^P = 800$  N/m, which enables robustness to terrain height variations as demonstrated empirically in Section 7.4.

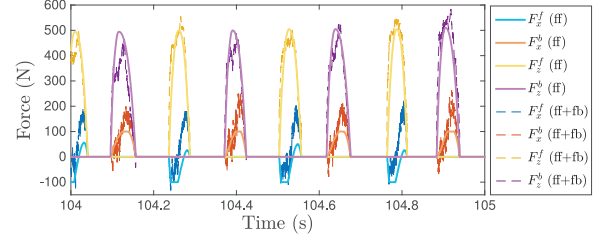


**Fig. 21.** Desired sagittal plane forces when running at 6 m/s. Solid lines indicate the feedforward forces from vertical momentum and pitch moment scaling. Dashed lines represent forces with feedback included.

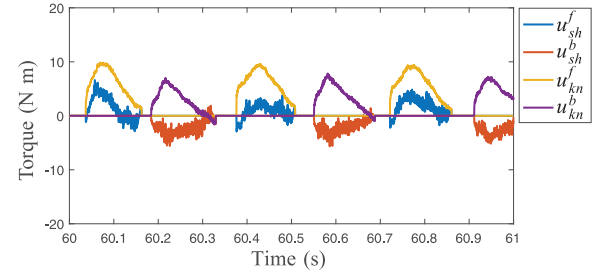


**Fig. 22.** Sagittal plane motor torques when running at 2 m/s. Torque values are quoted at the motor, prior to amplification by a 5.8:1 gearbox. The motors have a peak torque of approximately 30 N/m.

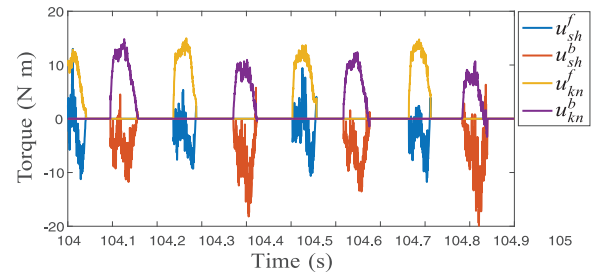


**Fig. 23.** Sagittal plane motor torques when running at 6 m/s. Torque values are quoted at the motor, prior to amplification by a 5.8:1 gearbox. The motors have a peak torque of approximately 30 N/m.

### 7.3. Power consumption

Figure 24 provides data on the power usage of the MIT Cheetah 2 for a separate experiment which was conducted with additional instrumentation to measure power flow out of the batteries. Thus, these numbers quantify the net energetic losses, not simply positive mechanical work (Seok et al., 2015). These numbers are provided mainly as documentation, as we conjecture they are due more-so to mechanical design rather than to control design. The power consumption exhibits significant variability from step to step at any given speed, as shown in Figure 24. The average cost of transport per step versus speed is also shown in Figure 24, with a minimum cost of transport of 0.47 achieved at 4 m/s. This figure represents a slight improvement over

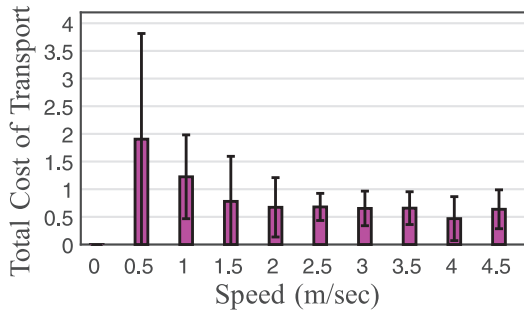
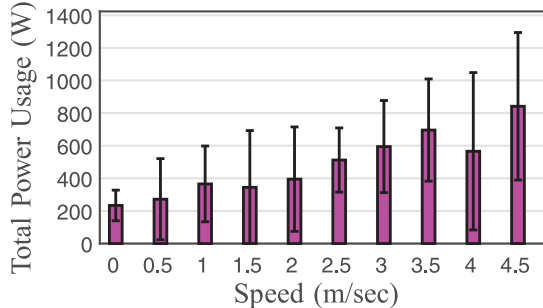


**Fig. 24.** Power usage and cost of transport (CoT) versus speed. The height of the bars represent the average and the solid lines represent +/- one standard deviation.

that the MIT Cheetah 1 robot (Seok et al., 2015), which had a cost of transport of 0.51.

#### 7.4. Empirical experimental stability and robustness

In this section, the stability and robustness of the controller is further demonstrated in environments with ground height variations, stiffness variations, and perturbations in state.

First, the controller was tested for robustness to ground height variations by placing various types of obstacles on the treadmill while running at 2.5 m/s. The robot was not provided with any information on the location or geometric properties of the obstacles. Figure 25 shows screen captures of an experimental video (see Extension 1). The obstacle types include 3/8 inch thick rubber tiles (Figure 25(a)), 2 inch thick polyurethane foam (Figure 25(b)), and a 1 × 4 inch wooden board (Figure 25(c)). The obstacles have different stiffnesses ranging from soft to rigid. The height perturbations introduced by these obstacles sometimes affect only a single foot, providing out-of-plane disturbances. In spite of placement of multiple obstacles, the robot was successfully able to run over the obstruction and return to its nominal running gait. A video of these results is provided in Extension 1.

The robot was also able to handle a wide range of ground stiffness without changing feedback gains or control parameters. The control design was tested on surfaces with different stiffnesses including very stiff grounds – a treadmill, paved surfaces, and an indoor running track, as well as soft grounds – a grassy field, dirt tracks, and an artificial turf

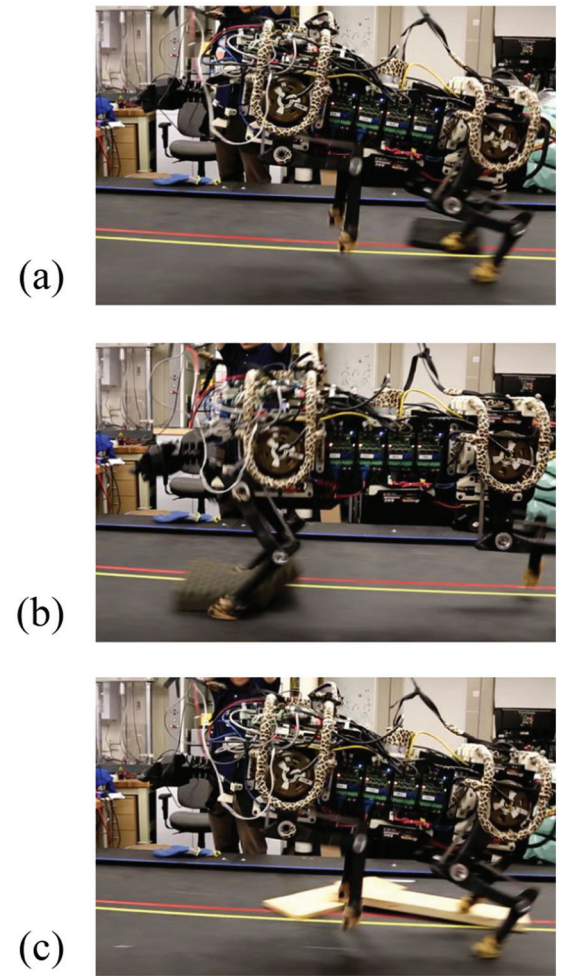


**Fig. 25.** MIT Cheetah 2 running over various types of obstacles, (a) rubber floor mats (b) polyurethane foam, and (c) 1 × 4 inch wooden boards. A full video is available in Extension 1.

field. Figure 1 shows screen captures of the experimental video, with clips of each terrain type provided in Extension 1. A preliminary version of the vertical impulse scaling algorithm has also shown robustness to handle rolling terrain as well as large steps in simulated galloping (Park and Kim, 2015). These combined results encourage expanded terrain robustness tests in future work.

The capability of the controller to handle large perturbations in state is further shown by experiments where the robot jumped over obstacles with heights up to 40 cm (Park et al., 2015b). While the autonomous jumping is not the focus of this work, stabilization upon landing, which includes handling deviations in state as well as gait pattern, is due to the control structure presented in this paper.

Figure 26 shows series of screen captures taken from the experimental video (see Extension 1) of the robot landing from jumping over an obstacle. The controller successfully recovered from state deviations away from the nominal gait as shown in Figure 27. This figure also shows the corresponding footfall patterns. Large perturbations to the gait

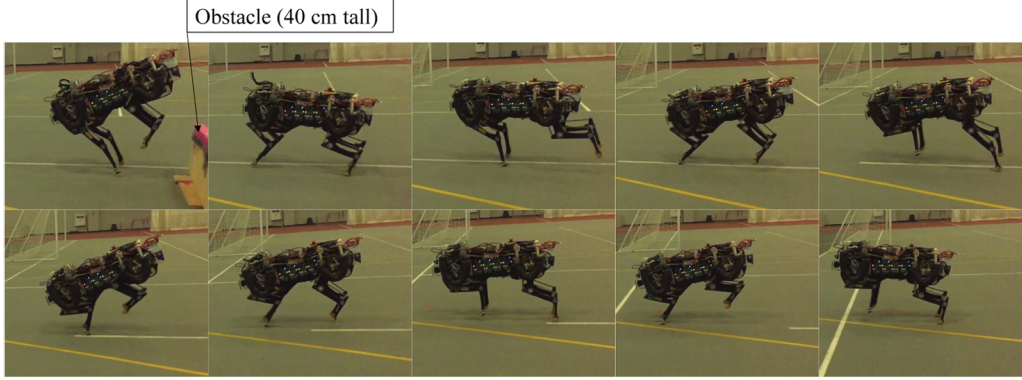


**Fig. 26.** MIT Cheetah 2 recovering to its nominal bounding gait following an initial state disturbance after a jumping motion. Snapshots proceed in time from left to right in the top row, then left to right in the bottom row. A full video is available in Extension 1.

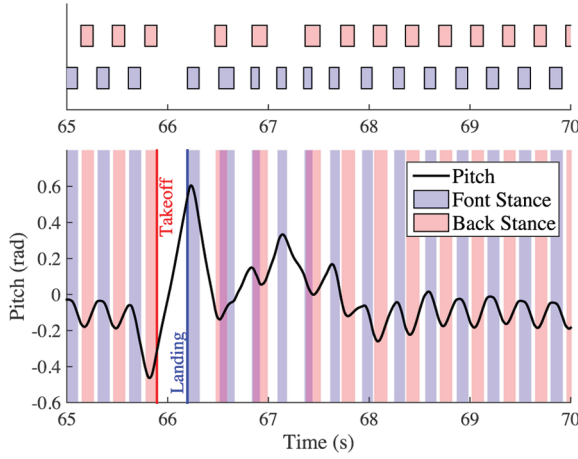


**Fig. 27.** Stabilization of the gait pattern and pitch following a jump over a 40 cm obstacle at  $t = 65.9$  s. The gait pattern stabilizer applied to the decoupled front and back leg state machines effectively handles periods of double support, as well as consecutive impacts by the same pair of legs, returning to the nominal pattern after approximately five steps.

pattern are caused by pitching from the jump. This leads to periods of double support and instances where the front feet touchdown twice between the footfalls of the back feet. These situations were not specifically addressed by the simple model analysis, yet the gait-pattern stabilizer and indirectly coupled leg state machines (Figure 15) handle them effectively. The gait pattern stabilizer successfully brings gait pattern back to steady state within approximately five steps. These results showcase the empirical robustness of the control framework.

## 8. Discussion

These results represent the state-of-the-art in 3D dynamic locomotion for electrically actuated quadrupeds. For legged machines to fulfill their intended roles outside of the

laboratory, however, yet higher degrees of robustness, versatility, and reliability must be pursued. These advances will undoubtedly occur through strategic and coordinated advances in actuation and sensing topologies, robust mechanical design, and a broader re-use of software across the community. We limit the scope of discussion here to our methods for control design and systems analysis.

Although the bounding gait is executed in 3D, its dynamics are dominated by the sagittal plane. Yet, some of the failures in the experiments were due to instability in roll and lateral velocity. In order to generate a wider set of gaits in 3D, the use of more general stability analysis tools in 3D would be helpful to guide the specification of 3D control gains.

A main limiting factor in pushing the performance envelope in our experiments was a fundamental lack of analysis tools to diagnose and correct failure modes. The full controller in experiments (Figure 11) includes contributions from many coupled modules, each running on different schedules. Pinpointing the root cause of failure, whether from an individual module, or from couplings, represented a significant challenge. Failures in the highest speed experiments would cost hundreds of dollars in replacement parts with repairs taking a few hours. Yet, often the causes of failure and appropriate patches were unable to be determined due to the challenges described above. Our existing tools for stability analysis provide only local guarantees, while predicated on models which will always be approximate. Moving forward, modular tools for robust control design and systems diagnosis represent a pressing challenge for large-scale experimental platforms.

The capabilities of available actuators were not a limiting factor in the performance of the bounding controller. Even at the highest speeds, Figure 23 shows that only 66% of the maximum actuator torque was used. Although our proprioceptive actuators top out at a 100 Hz control bandwidth (Wensing et al., 2016), the comparatively low bandwidth of force production in human muscle (Aaron and Stein, 1976) suggests that balance control strategies should not ultimately be limited by actuator bandwidth in our platform.

Biological locomotors widely use foot placement (Patla et al., 1999), a characteristically low-rate control approach limited by step frequency, to provide balance in response to disturbances or challenging terrains.

Footstep modification through capture point (Koolen et al., 2012) or Raibert-style heuristics (Raibert, 1986) has been used effectively in other legged robots. The modification of footprint locations shapes the set of forces and moments (also called the wrench cone) that can be placed on the body during stance (Escande et al., 2013). As a result, modification of footsteps allows, for instance, recovery of the body velocity without detriment to body posture. In this work, the short duration of the flight provided a challenge to track target footprint locations. Without footprint control, posture and speed were controlled entirely in stance through producing desired forces on the system. While this was shown to be effective, including footprint control represents an opportunity to provide additional stabilization mechanisms in future work. It is anticipated that these inclusions would tolerate yet larger disturbances and would reduce the force-bandwidth requirements in stance.

## 9. Conclusion

This paper has presented high-speed running results for the MIT Cheetah 2 robot. Results are enabled by impulse scaling principles to generalize the control of gait across a range of speeds. With this approach, a single set of control parameters is able to be used for the cheetah robot to run at speeds of 0.0 m/s to 6.4 m/s. The main control approach takes a common form of feedforward plus feedback control. However, the focus on momentum scaling principles enables the time-based feedforward component to only be based on easily identified system parameters such as total mass and inertia. When the timing of the feedforward forces are based purely on foot impacts, the gait pattern tends to drift. A gait pattern stabilizer has been presented which enables the robot to smoothly recover to the desired temporal footfall phasing through feedback on the foot impact times. A number of additional controller subsystems have been briefly presented in order to realize these algorithms in the experimental hardware. Energetic analysis shows the approach to result in efficient gaits with a minimum cost of transport of 0.47 at 4 m/s. This speed and efficiency represents a new level of performance for electrically actuated quadrupedal machines.

## Declaration of conflicting interests

The author(s) declared no potential conflicts of interest with respect to the research, authorship, and/or publication of this article.

## Funding

The author(s) disclosed receipt of the following financial support for the research, authorship, and/or publication of this article: This work was supported by the Defense Advanced Research Projects

Agency Maximum Mobility and Manipulation Program (grant number BAA-10-65-M3-FP-024), and the Agency for Defense Development of South Korea (grant number UD140073ID).

## Notes

1. The Froude number if given through  $Fr = v^2/gl$  where  $v$  is the forward velocity,  $g$  the gravitational constant, and  $l$  the nominal leg length. This nondimensional quantity allows for speed comparison in robots of different scales.
2. Note: This assumption is reasonable as the legs of the quadruped are very light, composing of approximately only 10% of the total mass of the system.
3. The wedge product effectively provides a cross product for vectors in  $\mathbb{R}^2$ . The cross product operator  $\times$  is reserved for application to vectors in  $\mathbb{R}^3$ , producing result in  $\mathbb{R}^3$ .

## References

- Aaron SL and Stein RB (1976) Comparison of an emg-controlled prosthesis and the normal human biceps brachii muscle. *American Journal of Physical Medicine & Rehabilitation* 55(1): 1–14.
- Barasuol V, Buchli J, Semini C, et al. (2013) A reactive controller framework for quadrupedal locomotion on challenging terrain. In: *IEEE international conference on robotics and automation*, Karlsruhe, Germany, 6–10 May 2013, pp.2554–2561.
- Bazeille S, Barasuol V, Focchi M, et al. (2014) Quadruped robot trotting over irregular terrain assisted by stereo-vision. *Intelligent Service Robotics* 7(2): 67–77.
- Blickhan R and Full R (1993) Similarity in multilegged locomotion: Bouncing like a monopode. *Journal of Comparative Physiology A* 173: 509–517.
- Chevallereau C, Grizzle JW and Shih CL (2009) Asymptotically stable walking of a five-link underactuated 3-D bipedal robot. *IEEE Transactions on Robotics* 25(1): 37–50.
- Coros S, Karpathy A, Jones B, et al. (2011) Locomotion skills for simulated quadrupeds. In: *Proceedings of ACM SIGGRAPH 2011*, 7–11 August 2011, vol. 30, no. 4, pp.59:1–12. Vancouver, British Columbia, Canada: ACM.
- Dai H, Valenzuela A and Tedrake R (2014) Whole-body motion planning with centroidal dynamics and full kinematics. In: *IEEE-RAS international conference on humanoid robots*. Madrid, Spain, 18–20 November 2014, pp.295–302.
- Escande A, Kheddar A and Miossec S (2013) Planning contact points for humanoid robots. *Robotics and Autonomous Systems* 61(5): 428–442.
- Full RJ and Koditschek DE (1999) Templates and anchors: Neuromechanical hypotheses of legged locomotion on land. *Journal of Experimental Biology* 202(23): 3325–3332.
- Gehring C, Coros S, Hutter M, et al. (2013) Control of dynamic gaits for a quadrupedal robot. In: *IEEE international conference on robotics and automation*, Karlsruhe, Germany, 6–10 May 2013, pp.3287–3292.
- Gehring C, Coros S, Hutter M, et al. (2014) Towards automatic discovery of agile gaits for quadrupedal robots. In: *IEEE international conference on robotics and automation*, Hong Kong, China, 31 May–7 June, pp.4243–4248.
- Herr HM and McMahon TA (2001) A galloping horse model. *The International Journal of Robotics Research* 20(1): 26–37.
- Hiskens IA (2001) Stability of hybrid system limit cycles: application to the compass gait biped robot. In: *IEEE conference*

- on decision and control*, vol. 1, Orlando, FL, 4–7 December, pp.774–779.
- Hiskens IA and Pai MA (2000) Trajectory sensitivity analysis of hybrid systems. *IEEE Transactions on Circuits and Systems I: Fundamental Theory and Applications* 47(2): 204–220.
- Hogan N (1985) Impedance control: An approach to manipulation: Part I—theory. *Journal of Dynamic Systems, Measurement, and Control* 107(1): 1–7.
- Hopkins MA, Hong DW and Leonessa A (2015) Compliant locomotion using whole-body control and divergent component of motion tracking. In: *IEEE International Conference on Robotics and Automation*, Seattle, WA, 26–30 May, pp.5726–5733.
- Hudson PE, Corr SA and Wilson AM (2012) High speed galloping in the cheetah (*acinonyx jubatus*) and the racing greyhound (*canis familiaris*): Spatio-temporal and kinetic characteristics. *The Journal of Experimental Biology* 215(14): 2425–2434.
- Hutter M (2013) *StarlETH & Co. – design and control of legged robots with compliant actuation*. PhD Thesis, ETH Zurich, Switzerland.
- Hutter M, Gehring C, Hopflinger M, et al. (2014a) Toward combining speed, efficiency, versatility, and robustness in an autonomous quadruped. *IEEE Transactions on Robotics* 30(6): 1427–1440.
- Hutter M, Sommer H, Gehring C, et al. (2014b) Quadrupedal locomotion using hierarchical operational space control. *The International Journal of Robotics Research* 33(8): 1047–1062.
- Hyun DJ, Seok S, Lee J, et al. (2014) High speed trot-running: Implementation of a hierarchical controller using proprioceptive impedance control on the MIT Cheetah. *The International Journal of Robotics Research* 33(11): 1417–1445.
- Kalakrishnan M, Buchli J, Pastor P, et al. (2011) Learning, planning, and control for quadruped locomotion over challenging terrain. *The International Journal of Robotics Research* 30(2): 236–258.
- Koolen T, de Boer T, Rebula J, et al. (2012) Capturability-based analysis and control of legged locomotion, Part 1: Theory and application to three simple gait models. *The International Journal of Robotics Research* 31(9): 1094–1113.
- Macchietto A, Zordan V and Shelton CR (2009) Momentum control for balance. In: *ACM SIGGRAPH*, New Orleans, LA, 3–7 August 2009, vol. 28, no. 3, pp.80:1–8.
- Maes LD, Herbin M, Hackert R, et al. (2008) Steady locomotion in dogs: Temporal and associated spatial coordination patterns and the effect of speed. *Journal of Experimental Biology* 211(1): 138–149.
- Mistry M, Buchli J and Schaal S (2010) Inverse dynamics control of floating base systems using orthogonal decomposition. In: *IEEE international conference on robotics and automation*, Anchorage, AK, 3–8 May 2010, pp.3406–3412.
- Mombaur K (2009) Using optimization to create self-stable human-like running. *Robotica* 27(3): 321–330.
- Nersesov S, Chellaboina V and Haddad WM (2002) A generalization of Poincaré's theorem to hybrid and impulsive dynamical systems. *International Journal of Hybrid Systems* 2: 39–55.
- Orin DE, Goswami A and Lee SH (2013) Centroidal dynamics of a humanoid robot. *Autonomous Robots* 35(2): 161–176.
- Ostrowski J and Burdick J (1996) Geometric perspectives on the mechanics and control of robotic locomotion. In: Giralt G and Hirzinger G (eds.) *Robotics Research*, Munich, Germany, 21–24 October 1995. London: Springer, DOI: 10.1007/978-1-4471-1021-7\_60.
- Palmer L and Orin D (2007) Force redistribution in a quadruped running trot. In: *IEEE international conference on robotics and automation*, Roma, Italy, 10–14 April 2007, pp.4343–4348.
- Park HW, Chuah MY and Kim S (2014) Quadruped bounding control with variable duty cycle via vertical impulse scaling. In: *IEEE/RSJ international conference on intelligent robots and systems*, Chicago, IL, 14–18 September 2014, pp.3245–3252.
- Park HW and Kim S (2015) Quadrupedal galloping control for a wide range of speed via vertical impulse scaling. *Bioinspiration & Biomimetics* 10(2): 025003.
- Park HW, Park S and Kim S (2015a) Variable-speed quadrupedal bounding using impulse planning: Untethered high-speed 3D running of MIT Cheetah 2. In: *IEEE international conference on robotics and automation*, Seattle, WA, 26–30 May 2015, pp.5163–5170.
- Park HW, Wensing P and Kim S (2015b) Online planning for autonomous running jumps over obstacles in high-speed quadrupeds. In: *Robotics: Science and systems*, Rome, Italy.
- Park J and Khatib O (2006) Contact consistent control framework for humanoid robots. In: *IEEE international conference on robotics and automation*, Orlando, FL, 15–19 May 2006, pp.1963–1969.
- Parker TS and Chua LO (1989) *Practical Numerical Algorithms for Chaotic Systems*. New York, Berlin: Springer.
- Patla AE, Prentice SD, Rietdyk S, et al. (1999) What guides the selection of alternate foot placement during locomotion in humans. *Experimental Brain Research* 128(4): 441–450.
- Poulakakis I, Papadopoulos E and Buehler M (2006) On the stability of the passive dynamics of quadrupedal running with a bounding gait. *International Journal of Robotics Research* 25(7): 669–687.
- Raiert M, Blankespoor K, Nelson G, et al. (2008) BigDog, the rough-terrain quadruped robot. In: *World congress of the international federation of automatic control*, Seoul, Korea, 6–11 July, vol. 41, no. 2, pp.10822–10825.
- Raiert MH (1986) *Legged Robots That Balance*. Cambridge, MA: MIT Press.
- Remy CD, Buffinton K and Siegwart R (2010) Stability analysis of passive dynamic walking of quadrupeds. *The International Journal of Robotics Research* 29(9): 1173–1185.
- Righetti L, Buchli J, Mistry M, et al. (2013) Optimal distribution of contact forces with inverse dynamics control. *The International Journal of Robotics Research* 32(3): 280–298.
- Righetti L, Mistry M, Buchli J, et al. (2011) Inverse dynamics control of floating-base robots with external constraints: A unified view. In: *IEEE international conference on robotics and automation*, Shanghai, China, 9–13 May 2011, pp.1085–1090.
- Rugh WJ (1996) *Linear Systems Theory*. 2nd ed. Upper Saddle River, NJ: Prentice-Hall, Inc.
- Semini C, Barasuol V, Boaventura T, et al. (2015) Towards versatile legged robots through active impedance control. *The International Journal of Robotics Research* 34(7): 1003–1020.
- Semini C, Tsagarakis NG, Guglielmino E, et al. (2011) Design of HyQ – a hydraulically and electrically actuated quadruped robot. *Proceedings of the Institution of Mechanical Engineers, Part I: Journal of Systems and Control Engineering* 225(6): 831–849.
- Sentis L, Park J and Khatib O (2010) Compliant control of multi-contact and center-of-mass behaviors in humanoid robots. *IEEE Transaction on Robotics* 26(3): 483–501.

- Seok S, Wang A, Chuah M, et al. (2015) Design principles for energy-efficient legged locomotion and implementation on the MIT Cheetah robot. *IEEE/ASME Transactions on Mechatronics* 20(3): 1117–1129.
- Seok S, Wang A, Otten D, et al. (2012) Actuator design for high force proprioceptive control in fast legged locomotion. In: *IEEE/RSJ international conference on Intelligent Robots and Systems*, Vilamoura, Portugal, 7–12 October 2012, pp.1970–1975.
- Sok KW, Yamane K, Lee J, et al. (2010) Editing dynamic human motions via momentum and force. In: *ACM SIGGRAPH/Eurographics symposium on computer animation*, Aire-la-Ville, Switzerland, 2–4 July 2010, pp.11–20. Madrid, Spain.
- Sreenath K, Park HW, Poulakakis I, et al. (2011) A compliant hybrid zero dynamics controller for stable, efficient and fast bipedal walking on mabel. *The International Journal of Robotics Research* 30(9): 1170–1193.
- Wensing PM and Orin DE (2016) Improved computation of the humanoid centroidal dynamics and application in dynamic whole-body control. *International Journal of Humanoid Robotics* 13(1): 1550039-1–1550039-23.
- Wensing PM, Palmer LR and Orin DE (2015) Efficient recursive dynamics algorithms for operational-space control with application to legged locomotion. *Autonomous Robots* 38(4): 363–381.
- Wensing PM, Wang A, Seok S, et al. (2016) Proprioceptive actuator design in the MIT cheetah: Impact mitigation and high-bandwidth physical interaction for dynamic legged robots. *IEEE Transactions on Robotics*. DOI: 10.1109/TRO.2016.2640183.
- Wieber PB (2006) Fast motions in biomechanics and robotics: Optimization and feedback control. In: *Holonomy and Non-holonomy in the Dynamics of Articulated Motion*. Heidelberg: Springer Berlin, pp.411–425.
- Winkler A, Havoutis I, Bazeille S, et al. (2014) Path planning with force-based foothold adaptation and virtual model control for torque controlled quadruped robots. In: *IEEE international conference on robotics and automation*, Hong Kong, China, 31 May–7 June 2014, pp.6476–6482.

## Appendix 1

### *Index to multimedia extensions*

Archives of IJRR multimedia extensions published prior to 2014 can be found at <http://www.ijrr.org>, after 2014 all videos are available on the IJRR YouTube channel at <http://www.youtube.com/user/ijrrmultimedia>

#### Table of Multimedia Extension

Extension	Media type	Description
1	Video	A video of experimental results from Section 7.

## Appendix 2

### *Notation*

Throughout the text, the set of real and complex numbers are denoted by  $\mathbb{R}$  and  $\mathbb{C}$  respectively. The set of

**Table 2.** Notation describing common variables and the qualifications provided through their sub/superscripts throughout the text.

Symbol	Definition
$m, I$	Total mass and pitch moment of inertia about CoM
$\mathbf{p} = (x, z)$	CoM position in the sagittal plane
$\psi, \theta, \phi$	Roll, pitch, and yaw angles
$\mathbf{q} = (x, z, \theta)$	Sagittal plane state
$\mathbf{F} = (F_x, F_z)$	Force applied in sagittal plane
$\tau$	Torque about CoM
$T$	Fixed gait timing parameter
$\bar{t}$	Time since beginning of current phase
$s$	Normalized phase time
$\alpha$	Ground reaction force/torque scaling coefficient
$\beta$	Bézier coefficient vector
$\mathbf{x}$	State of abstract bounding model
$\xi$	Controller parameter vector
$v_d$	Desired speed
$L$	Nominal stride length
$k, \kappa$	Gain
Sub/superscript	Definition
$f, b$	Front and back legs
$x, y, z$	Components in $x, y$ , and $z$ directions
$d$	Desired quantity
$st, sw, ai$	Stance, swing, and aerial phases
$P, D$	Proportional and derivative gain
$sh, kn, ab$	Shank, knee, and ab/ad degree of freedom within a leg
$L, R$	Left and right legs
$B$	Body
$*$	Nominal value
$corr$	Corrected desired value

non-negative reals is  $\mathbb{R}_+ := \{x \in \mathbb{R} \text{ s.t. } x \geq 0\}$ , while the set  $\mathbb{R}^n$  represents the set of  $n$ -tuples in  $\mathbb{R}$  – that is,  $\mathbb{R}^n := \{(a_1, \dots, a_n) \text{ s.t. } a_i \in \mathbb{R} \forall i \in \{1, \dots, n\}\}$ . Similarly  $\mathbb{R}^{m \times n}$  represents the set of all  $m \times n$  matrices with real valued entries. Unless otherwise specified, scalars and scalar valued quantities are denoted with italics ( $a, b, c, \dots$ ) while vectors and vector valued functions are denoted with upright bold ( $\mathbf{a}, \mathbf{b}, \mathbf{c}, \dots$ ). Matrix quantities are denoted with upright bold capitals ( $\mathbf{A}, \mathbf{B}, \dots$ ). For a square matrix,  $\mathbf{A} \in \mathbb{R}^{n \times n}$ , the characteristic polynomial of  $\mathbf{A}$  is defined by  $p_{\mathbf{A}}(\lambda) = \det(\lambda \mathbf{I}_{n \times n} - \mathbf{A})$  where  $\mathbf{I}_{n \times n}$  is the identity matrix in  $\mathbb{R}^{n \times n}$ . The roots of this polynomial (the eigenvalues of  $\mathbf{A}$ ) are denoted by the set  $\sigma_{\mathbf{A}} := \{\lambda \in \mathbb{C} \text{ s.t. } p_{\mathbf{A}}(\lambda) = 0\}$ , with the spectral radius specified as  $\rho(\mathbf{A}) := \max(\{|\lambda| \text{ s.t. } \lambda \in \sigma_{\mathbf{A}}\})$ . The tangent bundle of a manifold  $\mathcal{Q}$  is denoted as  $T\mathcal{Q}$ . Table 2 details common symbols, subscripts, and superscripts used throughout the text.

## Appendix 3

### Proof of Proposition 1

The conditions given by equations (6) and (7) provide periodicity in  $\dot{z}$  and  $\dot{\theta}$ . This can be easily checked by integrating the first two equations in equation (5). The existence of initial conditions which admit periodicity in  $\theta$  and  $z$  is also verified by twice integrating the first two equations in equation (5) to obtain the expression of  $\theta(t)$  and  $z(t)$ .

Suppose we are given  $F_z^*(t)$  and  $\tau^*(t)$  such that equations (6), (7), and (8) are satisfied. Let  $\theta^*(t)$  and  $z^*(t)$  provide any periodic orbit in  $\theta$  and  $z$ .

Letting  $\beta(t) := F_z^*(t)/z^*(t)$  and combining phases 1 and 2, and phases 3 and 4 for the hybrid bounding model, we view these periodic angular and vertical forced dynamics as a time-varying input to the remnant dynamics on  $\eta(t) := [x(t), \dot{x}(t)]^T$  as

$$\dot{\eta}(t) = \mathbf{A}(t) \eta(t) + \begin{bmatrix} 0 \\ \frac{\tau^*(t)}{z^*(t)} \end{bmatrix} \quad (61)$$

where

$$\mathbf{A}(t) := \begin{bmatrix} 0 & 1 \\ \beta(t) & 0 \end{bmatrix} \quad (62)$$

We consider searching for an orbit which begins immediately before the end of phase 4 and continues through two reset maps at times  $t_4$  and  $t_2$ . At each of these times, we can construct a full state before the reset map  $\mathbf{x}(t_i^-, \eta(t_i^-))$  from the remnant dynamic state  $\eta(t_i^-)$  and the periodic  $z^*(t_i^-), \theta^*(t_i^-)$ . This lifted state then allows the consideration of reset maps in the  $\eta$  space defined according to

$$\begin{aligned} \eta^+ &= \Delta_4^\eta(\eta^-) := \pi \circ \Delta_4(\mathbf{x}(t_4^-, \eta(t_4^-))) \\ \eta^+ &= \Delta_2^\eta(\eta^-) := \pi \circ \Delta_2(\mathbf{x}(t_2^-, \eta(t_2^-))) \end{aligned} \quad (63)$$

where  $\pi$  is the canonical projection selecting the remnant component of the state. The sensitivity of a trajectory to initial conditions for this system can be given by a monodromy matrix

$$\mathbf{X}(t) := \frac{\partial \eta(t; \eta_0)}{\partial \eta_0} \in \mathbb{R}^{2 \times 2}$$

The monodromy matrix can be obtained by numerically integrating the following linear time-varying system

$$\dot{\mathbf{X}}(t) = \mathbf{A}(t) \mathbf{X}(t) \quad (64)$$

during the continuous dynamics, with initial condition  $\mathbf{X}(0) = \mathbf{I}_{2 \times 2}$ . The following discrete map relates the monodromy matrix after and before any reset map

$$\mathbf{X}(t^+) = \frac{\partial \Delta_j^\eta(\eta^-)}{\partial \eta} \mathbf{X}(t^-)$$

where,  $t^+$  and  $t^-$  represent the time after and before the reset map, respectively. Without loss of generality, we can

consider the sensitivity of a trajectory to initial conditions before the reset map  $\Delta_4^\eta$ . If we define the state transition matrix  $\Phi(\tau_b, \tau_a)$  (Rugh, 1996) as the matrix obtained by integrating equation (64) over the interval of interest  $[\tau_a, \tau_b]$ , then, the monodromy matrix  $\mathbf{X}(T)$  can be given by

$$\mathbf{X}(T) = \Phi(T, t_2^+) \frac{\partial \Delta_2^\eta(\eta(t_2^-))}{\partial \eta} \Phi(t_2^-, 0) \frac{\partial \Delta_4^\eta(\eta(0))}{\partial \eta} \quad (65)$$

for the system in equation (61). Due to the structure of the reset maps  $\Delta_2^\eta(\eta^-)$  and  $\Delta_4^\eta(\eta^-)$ , the sensitivities across transitions are

$$\frac{\partial \Delta_4^\eta(\mathbf{x}^-)}{\partial \mathbf{x}} = \frac{\partial \Delta_2^\eta(\mathbf{x}^-)}{\partial \mathbf{x}} = \begin{bmatrix} 0 & 0 \\ 0 & 1 \end{bmatrix} \quad (66)$$

The state transition matrix  $\Phi(\tau_b, \tau_a)$  used in equation (65) can be expressed through the Peano-Baker series (Rugh, 1996)

$$\Phi(\tau_b, \tau_a) = \sum_{i=0}^{\infty} \mathbf{P}_i(\tau_b, \tau_a)$$

where  $\mathbf{P}_0(\tau_b, \tau_a) = \mathbf{I}_{2 \times 2}$  and the remaining  $\mathbf{P}_i$  are defined recursively as

$$\mathbf{P}_{i+1}(\tau_b, \tau_a) = \int_{\tau_a}^{\tau_b} \mathbf{A}(s) \mathbf{P}_i(s) ds$$

Since  $\beta(t) \geq 0$ , it follows that

$$\mathbf{P}_1(\tau_b, \tau_a) = \begin{bmatrix} 0 & \zeta_1(\tau_b, \tau_a) \\ v_1(\tau_b, \tau_a) & 0 \end{bmatrix}$$

and

$$\mathbf{P}_2(\tau_b, \tau_a) = \begin{bmatrix} \sigma_2(\tau_b, \tau_a) & 0 \\ 0 & \rho_2(\tau_b, \tau_a) \end{bmatrix}$$

with  $\zeta_1(\tau_a, \tau_a) \geq 0$ ,  $v_1(\tau_a, \tau_a) \geq 0$ ,  $\sigma_2(\tau_a, \tau_a) \geq 0$ , and  $\rho_2(\tau_a, \tau_a) \geq 0$ . Furthermore, due to the non-negative entries in  $\mathbf{A}(t)$ , all functions  $\zeta, \sigma, \rho$ , and  $v$  are monotonically increasing in time.

In particular,  $\rho_2(\tau_b, \tau_a) = \int_{\tau_a}^{\tau_b} s \beta(s) ds$ , which provides  $\rho_2(\tau_b, \tau_a) > 0$ . The non-negativity of all entries in each  $\mathbf{P}_i(\tau_b, \tau_a)$  follows via induction. As a result

$$\begin{aligned} \Phi_{2,2}(T, t^+) &\geq 1 + \rho_2(T, t^+) > 1 \\ \Phi_{2,2}(t^-, 0) &\geq 1 + \rho_2(t^-, 0) > 1 \end{aligned} \quad (67)$$

where  $\Phi_{2,2}$  represents the entry in the second row and second column of the state transition matrix. From equation (65)

$$\mathbf{X}(T) = \begin{bmatrix} 0 & X_{1,2} \\ 0 & \Phi_{2,2}(T, t^+) \Phi_{2,2}(t^-, 0) \end{bmatrix}$$

From equation (67),  $\Phi_{2,2}(T, t^+) \Phi_{2,2}(t^-, 0) > 1$ . Note that due to the Linear Time Varying (LTV) structure of equation (64) and the linearity of the reset maps given by equation

(66), this monodromy matrix provides an exact linear relationship between non-infinitesimal changes in initial conditions and their associated change in final state. It follows that there exists an initial condition  $\eta_0$  that exhibits  $T$  periodicity in the remnant dynamics, which guarantees an orbit lifted to the  $\mathbf{x}$  dynamics as well.

## Appendix 4

### Proof of Corollary 1

Since horizontal velocity does not affect the pitch and vertical dynamics, it follows that any unstable horizontal velocity dynamics from step to step in the reduced state  $\eta$  would extend to unstable  $\dot{x}$  dynamics from step to step in the full state  $\mathbf{x}$ . It was shown in Appendix 3 that the monodromy matrix  $\mathbf{X}(T)$  corresponding to these  $\eta$  dynamics contains an eigenvalue  $\Phi_{2,2}(T, t^+) \Phi_{2,2}(t^-, 0)$  which is greater than 1 from equation (67). Thus, the horizontal velocity dynamics from step to step are unstable.

## Appendix 5

### Bézier swing parameters for the extended bounding model

$$\boldsymbol{\beta}_x^{\text{sw}} = [-0.2, -0.259, -0.275, -0.384, 0.261, -0.017, 0.248, 0.267, 0.259, 0.2] \quad (68)$$

$$\boldsymbol{\beta}_z^{\text{sw}} = [-0.5, -0.45, -0.406, -0.065, -1.031, 0.095, -0.545, -0.374, -0.45, -0.5] \quad (69)$$

## Appendix 6

### Proof of Proposition 2

The gait pattern stabilizer from the main text modifies the stance time of each foot based on the error in relative timing between footfalls. Given an  $N$ -beat gait, this pattern stabilizer can be generalized as

$$T_{\text{st}}^1[k] = T_{\text{st}}^{1*} - \kappa(t_1[k] - t_N[k-1] - t_1^d) \quad (70)$$

$$T_{\text{st}}^2[k] = T_{\text{st}}^{2*} - \kappa(t_2[k] - t_1[k] - t_2^d) \quad (71)$$

$$T_{\text{st}}^3[k] = T_{\text{st}}^{3*} - \kappa(t_3[k] - t_2[k] - t_3^d) \quad (72)$$

$$\vdots \quad (73)$$

$$T_{\text{st}}^N[k] = T_{\text{st}}^{N*} - \kappa(t_N[k] - t_{N-1}[k] - t_N^d) \quad (74)$$

where  $T_{\text{st}}^i[k]$  is the stance duration for foot  $i$  following its  $k$ th footfall,  $t_i[k]$  is the time of its  $k$ th footfall, and  $t_i^d$  is the desired time between the fall of foot  $i$  and its predecessor. Assuming that each subsequent swing phase lasts  $T_{\text{sw}}^i = T - T_{\text{st}}^{i*}$  in length, the impact times then evolve as

$$t_i[k+1] = T + t_i[k] - \kappa e_i[k] \quad (75)$$

where

$$e_1[k] = t_1[k] - t_N[k-1] - t_1^d \quad (76)$$

$$e_i[k] = t_i[k] - t_{i-1}[k] - t_i^d \quad i \in \{2, \dots, N\} \quad (77)$$

These gait errors have a helpful telescoping property

$$\sum_{i=2}^N e_i[k] = t_N[k] - t_1[k] - T + t_1^d$$

Using this fact, the error dynamics evolve as

$$e_1[k+1] = T + t_1[k] - \kappa e_1[k] - t_N[k] - t_1^d \quad (78)$$

$$= - \sum_{i=2}^N e_i[k] - \kappa e_1[k] \quad (79)$$

$$= - \sum_{i=1}^N e_i[k] + (1 - \kappa) e_1[k] \quad (80)$$

$$e_i[k+1] = (1 - \kappa) e_i[k] + \kappa e_{i-1}[k] \quad i \in \{2, \dots, N\} \quad (81)$$

Thus, the gait pattern stabilizer error dynamics follow

$$\mathbf{e}[k+1] = \underbrace{\begin{bmatrix} -1 & -1 & -1 & \cdots & -1 \\ \kappa & 0 & 0 & \cdots & 0 \\ 0 & \kappa & 0 & & \vdots \\ \vdots & \ddots & \ddots & \ddots & 0 \\ 0 & \cdots & 0 & \kappa & 0 \end{bmatrix}}_{\mathbf{A}_1} \mathbf{e}[k] + (1 - \kappa) \mathbf{e}[k] \quad (82)$$

We let  $\mathbf{A} = \mathbf{A}_1 + (1 - \kappa) \mathbf{I}$  so that  $\mathbf{e}[k+1] = \mathbf{A} \mathbf{e}[k]$ .

The matrix  $\mathbf{A}_1$  has a characteristic polynomial

$$p_{\mathbf{A}_1}(\lambda) = \lambda^n + \lambda^{n-1} + \kappa \lambda^{n-2} + \cdots + \kappa^{n-1} \lambda^0$$

and  $p_{\mathbf{A}}(\lambda) = p_{\mathbf{A}_1}(\lambda - (1 - \kappa))$ . We note that  $1 \notin \sigma_{\mathbf{A}}$  since  $p_{\mathbf{A}_1}(\kappa) \neq 0$ . The characteristic polynomial of  $\mathbf{A}_1$  further has a helpful simplifying property

$$(\lambda - \kappa) p_{\mathbf{A}_1}(\lambda) = \lambda^{n+1} + (1 - \kappa) \lambda^n - \kappa^n \quad (83)$$

$$= \lambda^n (\lambda + (1 - \kappa)) - \kappa^n \quad (84)$$

When  $\kappa \in (0, 1)$  and  $\lambda^* \in \sigma_{\mathbf{A}}$  it follows that  $|\lambda^*| < 1$ . To show this, suppose instead that  $|\lambda^*| \geq 1$

$$0 = p_{\mathbf{A}}(\lambda^*) \quad (85)$$

$$= p_{\mathbf{A}_1}(\lambda^* - (1 - \kappa)) \quad (86)$$

$$= (\lambda - \kappa) p_{\mathbf{A}_1}(\lambda) \Big|_{\lambda=\lambda^*-(1-\kappa)} \quad (87)$$

$$= \lambda^n (\lambda + (1 - \kappa)) - \kappa^n \Big|_{\lambda=\lambda^*-(1-\kappa)} \quad (88)$$

$$= (\lambda^* - (1 - \kappa))^n \lambda^* - \kappa^n \quad (89)$$

Thus

$$(\lambda^* - (1 - \kappa))^n \lambda^* = \kappa^n \quad (90)$$

Taking norms and  $n$ th roots in equation (90) gives

$$|\lambda^* - (1 - \kappa)| = \kappa / |\lambda^*|^{\frac{1}{n}} \leq \kappa$$

The set  $\{\lambda \in \mathbb{C} \text{ s.t. } |\lambda - (1 - \kappa)| \leq \kappa\}$  is a closed region of radius  $\kappa$ , centered at  $1 - \kappa$  in  $\mathbb{C}$ . This set is contained within the unit circle, and intersects the unit circle at a single point,  $\lambda = 1$ . Since  $|\lambda^*| \geq 1$ , this implies that  $\lambda^* = 1$ , which is a contradiction, since  $1 \notin \sigma_A$ .

As a result, the error dynamics given by equation (82) have an asymptotically stable equilibrium at the origin. That is, for any initial conditions, if each subsequent swing phase takes its nominal time  $T_{sw}^i = T - T_{st}^{i*}$ , then the gait timing errors satisfy  $\mathbf{e}[k] \rightarrow 0$  as  $k \rightarrow \infty$ .